https://doi.org/10.5194/egusphere-2026-1134
Preprint. Discussion started: 9 March 2026

TANGO CO_2 and NO_2 Observations: Synergistic Usage to Improve Emission Quantification and Characterize Atmospheric Chemistry

Tobias Borsdorff[1], Maarten Krol[2], Pepijn Veefkind[3], and Jochen Landgraf[1]

[1]Space Research Organisation Netherlands, SRON, Leiden, the Netherlands
[2]Wageningen University & Research, WUR, Wageningen, the Netherlands
[3]Royal Netherlands Meteorological Institute, KNMI, De Bilt, the Netherlands

Correspondence: Tobias Borsdorff (t.borsdorff@sron.nl)

Abstract. The Twin Anthropogenic Greenhouse Gas Observers (TANGO) mission, scheduled for launch in 2028, will observe CO_2, CH_4, and NO_2 emission plumes from more than 10,000 industrial facilities per year using two formation-flying CubeSats. Here, NO_2 plume structures exhibit substantially lower random noise than the corresponding CO_2 features, motivating a synergistic exploitation of both species for improved emission quantification and for enhanced characterization of atmospheric chemistry within plumes. Using large-eddy simulations in combination with the Integrated Mass Enhancement (IME) method, we assess NO_2-based masking of CO_2 plumes for emission rates in the range 2.0–12.5 Mt yr^{-1}. This yields CO_2 emission estimates with precisions between 18.5 % and 3.4 %, depending on the emission strength, and corresponding absolute biases that decrease from 15.3 % to 2.4 %. As an alternative approach, we analyze the observed CO_2/NO_2 ratio. By fitting an empirical model to measurement simulations of this ratio and subsequently reconstructing the CO_2 plume from NO_2 observations, we obtain a substantial reduction in the apparent noise of the reconstructed CO_2 plume. For the inferred emission rates, however, the precision remains largely unchanged. Consequently, despite reduced errors in individual pixel-level observations, plume reconstruction does not enhance the precision of CO_2 emission estimates, because it converts originally uncorrelated pixel noise into spatially correlated errors. Neglecting these spatial error correlations leads to a severe underestimation of the retrieval uncertainty. A key advantage of the empirical CO_2/NO_2 ratio model is its ability to characterize plume chemistry. Here CO_2 serves as non-decaying reference tracer. We demonstrate that an effective timescale for the $NO \rightarrow NO_2$ conversion in emission plumes can be inferred for sources with CO_2 emissions > 5.0 Mt yr^{-1}. Application of the method to Environmental Mapping and Analysis Program (EnMAP) observations demonstrates its practical utility, confirming its applicability to real satellite data.

1 Introduction

Accurate monitoring of anthropogenic greenhouse gas and air pollutant emissions is critical for climate mitigation strategies and air quality management (Lee and Romero, 2023; Friedlingstein et al., 2022). Industrial point sources, particularly power plants and large industrial facilities, emit substantial amounts of carbon dioxide (CO_2) and nitrogen oxides (NO_x), making them priority targets for emission verification and monitoring. Spaceborne trace gas measurements have proven valuable for detecting and quantifying such emissions from various satellite platforms (Nassar et al., 2021; Fioletov et al., 2025). Over

https://doi.org/10.5194/egusphere-2026-1134
Preprint. Discussion started: 9 March 2026

the past two decades, satellite missions have progressively enhanced the capability to observe these emissions. NASA's Orbiting Carbon Observatory-2 (OCO-2), launched in 2014, and OCO-3 aboard the International Space Station since 2019, have demonstrated the ability to detect and quantify CO_2 emissions from individual power plants (Nassar et al., 2022; Moeini et al., 2025). The TROPOspheric Monitoring Instrument (TROPOMI) aboard Sentinel-5P, operational since 2017, provides daily tropospheric NO_2 column densities at unprecedented spatial resolution of 3.5 km $\times$ 5.5 km with high signal-to-noise ratio (Veefkind et al., 2012; van Geffen et al., 2022), enabling detection and quantification of NO_x emissions from cities and power plants (Beirle et al., 2019; Lorente et al., 2019; Mols et al., 2026). The hyperspectral imaging satellite EnMAP, with 30 m spatial resolution, has recently demonstrated simultaneous observations of CO_2 and NO_2 plumes from power plants (Borger et al., 2025). Looking forward, Japan's GOSAT-GW satellite, successfully launched in June 2025, will provide simultaneous observations of CO_2, CH_4, and NO_2 with both wide-area (10 km resolution, 911 km swath) and focused (1–3 km resolution, 90 km swath) observation modes (Tanimoto et al., 2025), representing the first global platform for co-located greenhouse gas and air pollutant monitoring.

CO_2 observations from space typically suffer from low signal contrast due to high measurement noise compared to the CO_2 features to be interpreted. The long atmospheric lifetime of CO_2 combined with elevated background concentrations obscures the detection of local source-triggered enhancements (Reuter et al., 2019; Li et al., 2025). In contrast, NO_2 measurements benefit from low atmospheric background concentration, and sharper plume contrast due to the short lifetime of NO_x (Kuhlmann et al., 2021; Hakkarainen et al., 2023). These favorable measurement characteristics have led to multi-species approaches for emission quantification. Several of the previous studies use NO_2 measurements to detect and mask CO_2 plumes, exploiting the superior detectability of NO_2 signals (Kuhlmann et al., 2019; Reuter et al., 2019). Other methods convert NO_2 observations to NO_x and then infer CO_2 emissions using assumed or site-specific NO_x/CO_2 emission ratios (Zhang et al., 2023). Recent work has developed models to convert NO_2 to NO_x column densities that account for photochemical conversion along the plume using plume-resolving simulations (Meier et al., 2024) and methods that explicitly exploit signal-to-noise ratio differences between co-emitted trace gas species by transferring spatial information from high-SNR tracers (e.g., NO_2) to denoise low-SNR target species (Koene et al., 2025).

The upcoming Twin Anthropogenic Greenhouse Gas Observers (TANGO) mission, planned for launch in 2028, addresses the challenge of detecting small anthropogenic CO_2 enhancements through formation flight of two CubeSats, TANGO-Nitro and TANGO-Carbon. Both platforms observe the same scene within approximately 60 s (Day et al., 2023). Each satellite acquires measurements at a spatial resolution of 300 m across a 30 km swath, thereby enabling the synergistic analysis of the two species CO_2 and NO_2, the latter produced from NO emissions through photochemical reactions with O_3. TANGO's mission requirements specify detectability of CO_2 emissions for major point sources (>2.5 Mt CO_2 yr^{-1}) (Brenny et al., 2023), necessitating advanced data analysis methods to achieve this detection limit. Here, the NO_2 observations creates an opportunity to improve CO_2 emission estimates by combining information from both species. In this study, we investigate the synergistic exploitation of CO_2 and NO_2 observations for TANGO and similar missions. Using high-resolution large-eddy simulations from the MicroHH model with explicit atmospheric chemistry (van Heerwaarden et al., 2017; Krol et al., 2024), we evaluate two approaches across a range of CO_2 emissions from 2.0 to 12.5 Mt yr^{-1}. The first approach uses NO_2 observations to define

https://doi.org/10.5194/egusphere-2026-1134
Preprint. Discussion started: 9 March 2026

spatial masks for CO_2 integration, exploiting NO_2's superior signal-to-noise ratio for plume detection. The second approach fits an exponential model to the CO_2/NO_2 ratio. Multiplying the model with observed NO_2 fields yields a CO_2 fields with reduced noise. Moreover, the model provides chemistry parameters—specifically the NO→NO_2 conversion timescale τ_s, the apparent source ratio $m_1 + m_0$, and the far-field background ratio m_0—that characterize plume chemical evolution. We demonstrate that NO_2 plume masking provides superior emission estimates for CO_2 sources < 5 Mt yr^{-1}, while ratio reconstruction enables interpretable chemistry characterization for stronger emissions. Both methods are evaluated for robustness to realistic TANGO observing conditions including temporal separations up to 60 s and spatial misalignments up to 150 m, with validation using EnMAP satellite observations confirming real-world applicability.

This paper is structured as follows. Section 2 provides an overview of the TANGO mission, and Section 3 details the MicroHH simulation configuration as well as the methodology employed to generate synthetic TANGO observations. Section 4 describes the methods for the synergistic exploitation of CO_2 and NO_2 observations, including NO_2 plume masking and the CO_2/NO_2 ratio model framework. This section also addresses rigorous error propagation, explicitly accounting for error correlations. Section 5 quantifies emission uncertainties under idealized conditions, investigates the sensitivity to temporal and spatial measurement mismatches, assesses the retrieved chemical parameters, and demonstrates the methodology using EnMAP observations. Finally, Section 6 summarizes our findings and provides the conclusions of the study.

2 TANGO mission

The Twin Anthropogenic Greenhouse gas Observers (TANGO) mission is a forthcoming satellite campaign planned for launch in 2028 under the European Space Agency (ESA) SCOUT programme (Landgraf and Veefkind, 2025). The mission comprises two dedicated 16U CubeSats both operating in low Earth, sun-synchronous late-morning orbit at an altitude of approximately 500 km: TANGO-Carbon, designed to retrieve atmospheric concentrations of carbon dioxide (CO_2) and methane (CH_4), and TANGO-Nitro, dedicated to monitoring nitrogen dioxide (NO_2) emissions. The mission is specifically optimized to detect spatially confined CO_2, CH_4, and NO_2 emission plumes originating from localized point sources, such as power plants and landfills. TANGO-Carbon will record Earth radiance spectra in the 1.6 μm spectral domain (1590–1675 nm), with a spectral resolution of 0.45 nm and a sampling of 0.15 nm. The instrument is designed to detect CO_2 emission sources from single overpasses exceeding 2.5 Mt yr^{-1} and CH_4 sources greater than 5.0 kt yr^{-1}. TANGO-Nitro will operate in the visible range (400–500 nm) with a spectral resolution of 0.6 nm and a sampling of about 0.26 nm to support plume identification and characterization. The mission's agile pointing with a narrow swath of 30 km and a ground sampling distance of approximately 300 m are well suited for resolving and detecting highly localized emissions. Owing to their high pointing agility, the satellites can be rapidly repointed, enabling targeted observations of more than 10,000 individual emission sources per year (Landgraf and Veefkind, 2025; Charuvil Asokan et al., 2025). The temporal offset between measurements acquired by TANGO-Carbon and TANGO-Nitro is constrained to remain below 60 s. This stringent temporal co-registration facilitates quasi-simultaneous, co-located observations of CO_2 and NO_2 over the same emission sources, thereby improving the attribution of observed fluxes to specific facilities and enhancing the quantitative characterization of their emission signatures.

https://doi.org/10.5194/egusphere-2026-1134
Preprint. Discussion started: 9 March 2026

3 Data: Simulated TANGO measurements

To evaluate the upcoming TANGO mission capabilities, we require simulations with high spatial resolution that capture sub-kilometer turbulence features. At TANGO's 300 m resolution, turbulent eddies and plume meandering become observable and significantly affect column density distributions and emission estimates. We therefore perform large-eddy simulations (LES) of a coal-fired power plant using MicroHH (van Heerwaarden et al., 2017), which explicitly resolves energy-containing turbulent scales and includes atmospheric chemistry (Krol et al., 2024).

3.1 LES simulation setup

We employ high-resolution large-eddy simulations to generate realistic plume fields under controlled conditions where the true emission rates and atmospheric chemistry are known. The simulation domain spans 16.4 km $\times$ 8.2 km horizontally and extends 4.1 km vertically, covering approximately half of TANGO's along-track viewing domain while ensuring the entire plume remains within the field of view. The computational grid comprises $256 \times 128 \times 64$ cells, yielding 64 m horizontal and vertical sampling. This is approximately five times finer than TANGO's native 300 m resolution, ensuring proper representation of the turbulent cascade and inertial sub-range while providing realistic small-scale variability that will be smoothed by the instrument spatial response function.

Our base case is a synthetic emission source $(x_0, y_0, z_0) = (1024, 4096, 200)\,\mathrm{m}$ that represents a mid-sized coal-fired power plant. Emissions are distributed spatially using Gaussian profiles with 50 m standard deviation to represent dispersion from a stack. The source emits CO_2, NO, NO_2, CO, and C_3H_6 with rates representative of typical coal combustion: CO_2 = 9.0 kmol s^{-1} (12.5 Mt yr^{-1}), NO = 0.0203 kmol s^{-1}, NO_2 = 0.00107 kmol s^{-1}, CO = 0.001135 kmol s^{-1}, and C_3H_6 = 0.000119 kmol s^{-1} (Krol et al., 2024). A constant west-to-east wind of 5 m s^{-1} is imposed uniformly throughout the domain, and the background atmosphere is initialized with 30 ppb O_3, which drives photochemical conversion of NO to NO_2 through the reaction NO + O_3 $\rightarrow$ NO_2 + O_2, while background NO and NO_2 concentrations are initialized to 0.05 ppb and 0.1 ppb, respectively. After allowing sufficient time for turbulence to develop and reach a quasi-steady state, we extract 10 independent plume realizations at 1-minute intervals. This temporal sampling strategy serves two purposes: providing multiple plume structures for uncertainty analysis, and enabling assessment of how temporal offsets between CO_2 and NO_2 observations affect reconstruction performance when the satellites do not measure simultaneously.

To investigate performance across different emission strengths, we generated two additional simulation sets by uniformly scaling all emission rates of our base case (CO_2, NO, NO_2, CO, and C_3H_6) by constant factors while keeping all other atmospheric and meteorological conditions identical. This approach maintains realistic emission ratios and plume chemistry while varying signal strength. This results in the four plume cases in this study corresponding to CO_2 emission rates of 1.44 kmol s^{-1} (2.0 Mt yr^{-1}), 1.8 kmol s^{-1} (2.5 Mt yr^{-1}), 3.6 kmol s^{-1} (5.0 Mt yr^{-1}), and 9 kmol s^{-1} (12.5 Mt yr^{-1}), representing small, medium, and large industrial facilities within TANGO's target range. By scaling the emission of all species proportionally rather than adjusting CO_2 alone, the NO_x/CO_2 emission ratios remain fixed across cases. Note, however, that the chemical

https://doi.org/10.5194/egusphere-2026-1134
Preprint. Discussion started: 9 March 2026

regime is not strictly invariant: higher NO_x emissions lead to stronger O_3 titration, which non-linearly affects the $NO \rightarrow NO_2$ conversion timescale. The CO_2 scaling is purely linear and affects results primarily through the signal-to-noise ratio.

3.2 Synthetic TANGO observations

Figure 1 shows a representative snapshot from the LES for the 12.5 Mt yr^{-1} emission case. Panel (a) displays CO_2 column density, peaking at the source location with characteristic turbulent plume structure. Panel (c) shows NO column density, also maximizing at the source. Panel (b) shows NO_2 column density, with maximum enhancement several kilometers downwind due to chemical conversion from NO to NO_2 during advection. Panel (d) indicates O_3 depletion along the plume from NO titration reactions. The spatial offset between CO_2 and NO_2 enhancement maxima demonstrates the coupled turbulent-chemical processes that TANGO will observe.

To emulate TANGO measurements, MicroHH fields are processed through an observation operator that includes (1) vertical integration to obtain column densities, (2) convolution with a 2D Gaussian point spread function (300 m FWHM) to simulate instrument spatial response, and (3) data sampling on $300\ \mathrm{m} \times 300\ \mathrm{m}$ pixels. CO_2 and NO_2 can be sampled on spatially offset grids or from different temporal snapshots, simulating asynchronous observations expected from the two-satellite configuration. Finally, Gaussian measurement noise is added based on TANGO mission requirements: 0.576 mol m^{-2} for CO_2 (approximately 1 % of the 420 ppm atmospheric background column) and 3.75×10^{-5} mol m^{-2} for NO_2. Considering the maximum plume enhancements with respect to the atmospheric background, the NO_2 measurements exhibit approximately four times higher signal-to-noise ratio compared to CO_2. Figure 2a,b displays an example plume for the 12.5 Mt yr^{-1} case after down-sampling to 300 m resolution and adding TANGO-representative measurement noise. These synthetic observations serve as the basis for Monte Carlo experiments as well as linear error propagation analyses to evaluate emission estimation performance and quantify uncertainties under various operational scenarios.

4 Methodology

To investigate the CO_2–NO_2 synergy of the TANGO observation concept, we exploit co-located CO_2 and NO_2 satellite observations to improve emission quantification and characterize atmospheric chemistry. The method leverages the typically higher signal-to-noise ratio of NO_2 plumes compared to CO_2 plumes at fine spatial resolution by empirically modeling the downwind evolution of the CO_2/NO_2 ratio. This section describes the ratio-based reconstruction approach and a simpler NO_2-based plume masking method, the Integrated Mass Enhancement (IME) technique for emission estimation, and the rigorous error propagation framework accounting for spatial correlations. Performance evaluation is presented in Section 5. Throughout this section, CO_2 and NO_2 denote retrieved column densities (mol m^{-2}) after background subtraction. The approaches require CO_2 and NO_2 observations on a common spatial grid. When original retrievals are provided on different grids—as will be the case for TANGO's two formation-flying satellites—the NO_2 field is interpolated onto the CO_2 grid using smooth cubic spline interpolation. Figure 2a,b shows the CO_2 and NO_2 measurements for the 12.5 Mt yr^{-1} case with typical measurement noise, as described in Section 3.2.

https://doi.org/10.5194/egusphere-2026-1134
Preprint. Discussion started: 9 March 2026

4.1 CO_2/NO_2 ratio model

To account for atmospheric conversion of NO to NO_2 and dilution downwind of an industrial source, the CO_2/NO_2 ratio is modeled by an exponential function (Meier et al., 2024):

$$F(s;\mathbf{x}) = m_1 \exp\left(-\frac{s}{\tau_d}\right) + m_0, \tag{1}$$

Here, s denotes the downwind Euclidean distance from the emission source, τ_d is the characteristic spatial decay length scale, m_1 is the initial amplitude of the ratio, and m_0 represents the asymptotic background value. The exponential parameterization represents the dominant physical processes: elevated CO_2/NO_2 ratios in the vicinity of the source (arising from direct CO_2 emissions and the initially limited formation of NO_2), followed by an exponential decrease as NO is oxidized to NO_2 and both species are subject to turbulent dilution. The three parameters τ_d, m_0, and m_1 that are summarized in a state vector

$$\mathbf{x} = (\tau_d, m_0, m_1)^T\,, \tag{2}$$

provide quantitative, observation-based characterization of plume chemical evolution. The spatial decay parameter τ_d yields an effective chemical timescale when divided by the wind speed, the apparent source ratio $m_1 + m_0$ characterizes the CO_2/NO_2 ratio at the emission location, and m_0 represents the background CO_2/NO_2 ratio downwind. Physical interpretation of these parameters is discussed in Section 5.

4.2 Ratio model fitting

To fit the model in Eq. (1) to observations, we first define the unitless ratio

$$y_i = \frac{[\mathrm{CO_2}]_\mathrm{i}}{[\mathrm{NO_2}]_\mathrm{i}}, \tag{3}$$

as observable where $[\mathrm{CO_2}]_i$ and $[\mathrm{NO_2}]_i$ are the total column densities of the corresponding trace gases at spatial sampling point i. Assuming uncorrelated Gaussian measurement errors in CO_2 and NO_2 with standard deviations $\sigma_{i,\mathrm{CO_2}}$ and $\sigma_{i,\mathrm{NO_2}}$, the precision in y_i is obtained via standard error propagation:

$$\frac{\sigma_{y_i}^2}{y_i^2} = \frac{\sigma_{i,\mathrm{CO_2}}^2}{[\mathrm{CO_2}]_\mathrm{i}^2} + \frac{\sigma_{i,\mathrm{NO_2}}^2}{[\mathrm{NO_2}]_i^2}. \tag{4}$$

For the measurement vector $\mathbf{y} = (y_1, \cdots, y_N)$, the corresponding error covariance matrix is given by

$$\mathbf{S}_y = \mathrm{diag}(\sigma_{y_1}^2, \ldots, \sigma_{y_N}^2)\,. \tag{5}$$

In the following, we assume that the measured ratio $\mathbf{y}$ can be represented by our model $F(s_i;\mathbf{x})$, evaluated at the distance s_i between the sampling point i of the observation and the source location. This implicitly neglects a potential model bias arising from the fact that F describes the ratio of the underlying physical CO_2 and NO_2 fields, whereas the measurement $\mathbf{y}$ is a ratio

https://doi.org/10.5194/egusphere-2026-1134
Preprint. Discussion started: 9 March 2026

of observed quantities whose numerator and denominator each correspond to a convolution of the true physical fields with the instrument's spatial response function. The higher the spatial resolution of the sensor, the smaller this bias is expected to be. In the following, we assume that for the TANGO spatial resolution of 300 m this error can be neglected; however, we will revisit this assumption when discussing systematic biases in the retrieved components of the state vector. Under this assumption, the state vector in Eq. (2) is estimated by minimizing the weighted least-squares cost function (Hansen, 2010):

$$\mathbf{x}_{\mathrm{ret}} = \min_{\mathbf{x}} \left\{ (\mathbf{y} - \mathbf{F}(\mathbf{x}))^{\mathrm{T}} \mathbf{S}_y^{-1} (\mathbf{y} - \mathbf{F}(\mathbf{x})) \right\}, \tag{6}$$

where $\mathbf{F}(\mathbf{x})$ is the forward model vector with elements $F(s_i;\mathbf{x})$ for each pixel. The minimization is performed using a Gauss–Newton iterative scheme, where a linearized least squares problem is solved per iteration step. After convergence, the solution is

$$\mathbf{x}_{\mathrm{ret}} = \mathbf{G}\mathbf{y} \tag{7}$$

with the gain matrix

$$\mathbf{G} = (\mathbf{J}^{\mathrm{T}} \mathbf{S}_y^{-1} \mathbf{J})^{-1} \mathbf{J}^{\mathrm{T}} \mathbf{S}_y^{-1} \tag{8}$$

and the parameter covariance matrix

$$\mathbf{S}_x = (\mathbf{J}^{\mathrm{T}} \mathbf{S}_y^{-1} \mathbf{J})^{-1} . \tag{9}$$

The forward model Jacobian $\mathbf{J}$ with

$$J_{i,k} = \frac{\partial F(s_i;\mathbf{x})}{\partial x_k} \tag{10}$$

is calculated at the expansion point of the last iteration step.

To ensure robust fitting, we filter out pixels in the measurement vector $\mathbf{y}$ with insufficient signal-to-noise: specifically, pixels where

$$\frac{[\mathrm{NO_2}]_{\mathrm{i}}}{\sigma_{i,\mathrm{NO_2}}} < 2 \quad \text{or} \quad \frac{[\mathrm{CO_2}]_{\mathrm{i}}}{\sigma_{i,\mathrm{CO_2}}} < 2 \tag{11}$$

or where the unit-less ratio uncertainty σ_{y_i} exceeds a predefined threshold. In this study we choose a threshold of 50 % of the ratio value. Only pixels passing these criteria are included in the measurement vector. Figure 2d shows the modeled CO_2/NO_2 ratio using Eq. (1) for the 12.5 Mt yr^{-1} base case, illustrating how the model captures the essential chemistry and transport processes represented in the MicroHH simulation shown in Figure 2c. The model is applied directly to the CO_2/NO_2 ratio, so finite spatial resolution mainly affects the source ratio $m_1 + m_0$, while the decay scale τ_d and m_0 characterization is discussed in Section 5.

4.3 CO_2 plume reconstruction

After the model fit, a CO_2 field can be derived from the NO_2 measurements by

$$[\mathrm{CO_2}]_i^{\mathrm{recon}} = F(s_i;\mathbf{x}_{\mathrm{ret}}) \cdot [\mathrm{NO_2}]_{\mathrm{i}}. \tag{12}$$

https://doi.org/10.5194/egusphere-2026-1134
Preprint. Discussion started: 9 March 2026

The error covariance matrix $\mathbf{S}_{\mathrm{recon}}$ of the reconstructed $[\mathrm{CO_2}]^{\mathrm{recon}}$ field is given by

$$S_{\mathrm{recon},ij} = [\mathrm{NO_2}]_i\,[\mathrm{NO_2}]_j\,\mathbf{J}_i\,\mathbf{S}_x\,\mathbf{J}_j^{\mathrm{T}} + \delta_{ij}F^2(s_i;\mathbf{x}_{\mathrm{ret}})\,\sigma^2_{i,\mathrm{NO_2}}, \quad i,j = 1,\ldots,N, \tag{13}$$

where $\mathbf{J}_i$ denotes the i-th row of the Jacobian matrix $\mathbf{J}$, $\mathbf{S}_x$ is the covariance matrix of the fitted model parameters, $\sigma_{\mathrm{NO_2}}$ is the $\mathrm{NO_2}$ measurement noise standard deviation, and δ_{ij} is the Kronecker delta. The second term on the right-hand side of the equation describes uncorrelated $\mathrm{CO_2}$ errors due to a scaling of corresponding $\mathrm{NO_2}$ errors, whereas the first term describes correlated $\mathrm{CO_2}$ errors due to the errors on the model parameter x.

Figure 2e shows the reconstructed $\mathrm{CO_2}$ field for the 12.5 Mt yr^{-1} case, which exhibits reduced noise compared to the original $\mathrm{CO_2}$ measurement. The difference between the reconstructed and original $\mathrm{CO_2}$ fields (Figure 2f) primarily reflects the filtered measurement noise in the first term in Eq. (13). The implications of this noise reduction for integrated emission uncertainty are evaluated in Section 5. By design, the ratio model can represent only those spatial and temporal structures that are describable by the three fitted parameters. Consequently, systematic errors that are present in the $\mathrm{CO_2}$ column density product but absent in the corresponding $\mathrm{NO_2}$ field are substantially mitigated by the fitting procedure. For example, retrieval artifacts—such as striping or surface-related structures—that affect $\mathrm{CO_2}$ and $\mathrm{NO_2}$ differently are partially suppressed.

4.4 Sensitivity analysis

To assess the effective information content of the reconstruction, we compute the sensitivity of $\mathrm{CO_2^{recon}}$ to the true $\mathrm{CO_2}$ signal using a pixel-wise sensitivity matrix, analogous to an averaging kernel (Rodgers, 2000):

$$A_{ij} = \frac{\partial[\mathrm{CO_2}]^{\mathrm{recon}}_{\mathrm{i}}}{\partial[\mathrm{CO_2}]^{\mathrm{true}}_{\mathrm{j}}} = \frac{[\mathrm{NO_2}]_i}{[\mathrm{NO_2}]_{\mathrm{j}}} \cdot (\mathbf{J}\cdot\mathbf{G})_{ij}\,, \tag{14}$$

Matrix $\mathbf{A}$ quantifies how strongly $[\mathrm{CO_2}]^{\mathrm{recon}}$ responds to the true $[\mathrm{CO_2}]^{\mathrm{true}}$ signal:

$$[\mathrm{CO_2}]^{\mathrm{recon}} = \mathbf{A}\cdot[\mathrm{CO_2}]^{\mathrm{true}}. \tag{15}$$

The complementary term $1 - A_{ii}$ defines the fraction of the signal not captured by the model, representing the null-space error of the reconstruction approach (Borsdorff et al., 2014). This sensitivity analysis quantifies the extent to which the reconstructed $\mathrm{CO_2}$ field faithfully represents the true atmospheric state versus being influenced by the $\mathrm{NO_2}$ observations and model constraints.

Figure 3 illustrates the application of the averaging kernel $\mathbf{A}$ for the 12.5 Mt yr^{-1} base case. To stress-test the method, we define the true $\mathrm{CO_2}$ field as a plume from 9 minutes before the time step used to derive $\mathbf{A}$ (Fig. 3a); this represents an extreme case, as the temporal separation between $\mathrm{CO_2}$ and $\mathrm{NO_2}$ observations from TANGO will be less than 1 minute in practice. When $\mathbf{A}$ is applied to this earlier plume according to Eq. (15), the reconstructed field (Fig. 3b) exhibits turbulence patterns from the later $\mathrm{NO_2}$ plume used to construct $\mathbf{A}$, demonstrating that reconstruction always responds with the turbulence features of the $\mathrm{NO_2}$ field rather than the true $\mathrm{CO_2}$ field. The difference field (Fig. 3c) reveals this temporal mismatch in turbulent structures. This represents a fundamental limitation of the method: reconstruction performance depends critically on temporal alignment between $\mathrm{CO_2}$ and $\mathrm{NO_2}$ observations, degrading when $\mathrm{CO_2}$ and $\mathrm{NO_2}$ plume structures begin to de-correlate.

https://doi.org/10.5194/egusphere-2026-1134
Preprint. Discussion started: 9 March 2026

Although the 9-minute separation used here is far larger than what TANGO will experience, it serves to clearly expose this sensitivity. Quantitative evaluation of temporal separation effects, including sub-minute separations representative of TANGO, is presented in Section 5.

4.5 NO_2-based plume masking

As a simpler alternative to full reconstruction, NO_2 observations can be used to define a plume mask that identifies the spatial extent of the emission plume. A threshold is applied to the NO_2 field to identify pixels within the plume, and the CO_2 emission is then estimated by integrating only those CO_2 pixels that fall within this mask. This approach avoids the complexity of ratio fitting while still leveraging NO_2's superior signal-to-noise ratio for plume detection.

The masking threshold is chosen to balance two competing effects: setting the threshold too low includes background noise and increases random error, while setting it too high truncates the true plume extent and introduces systematic bias. An optimal threshold can be determined empirically by minimizing the total error (combining bias and random uncertainty). Performance evaluation and threshold optimization are presented in Section 5.

4.6 Emission estimation using the Integrated Mass Enhancement method

To estimate the total emission rate E, we employ the Integrated Mass Enhancement (IME) method (Santaren et al., 2025; Varon et al., 2018):

$$E = \frac{\Delta a}{t_{\mathrm{trans}}} \sum_{i \in I} [\mathrm{CO_2}]_i, \tag{16}$$

where I denotes pixels within the plume boundary, Δa is the pixel area (assumed constant), and $t_{\mathrm{trans}} = L/U$ is the plume transit time with U the effective mass-weighted wind speed and L the plume length along the wind direction.

For the reconstruction approach, $[\mathrm{CO_2}]_i$ is replaced by the reconstructed field $[\mathrm{CO_2}]_i^{\mathrm{recon}}$ from Eq. (12). For the masking approach, the original CO_2 observations are used, with the summation restricted to pixels identified by the NO_2-derived mask.

The precision σ_E of the flux estimate E is derived from the error covariance of the CO_2 field by

$$\sigma_E^2 = \mathbf{K}_{\mathrm{CO_2}}^{\mathrm{T}} \mathbf{S}_{\mathrm{CO_2}} \mathbf{K}_{\mathrm{CO_2}}, \tag{17}$$

where $\mathbf{K}_{i,\mathrm{CO_2}} = \partial E / \partial [\mathrm{CO_2}]_{\mathrm{i}} = \Delta a / t_{\mathrm{trans}}$ is the derivative linking each pixel's CO_2 value to the total emission, and $\mathbf{S}_{\mathrm{CO_2}}$ is the covariance of the CO_2 field. For reconstruction, $\mathbf{S}_{\mathrm{CO_2}} = \mathbf{S}_{\mathrm{recon}}$ from the previous subsection, which includes spatial correlations introduced by the ratio fitting. For masking, $\mathbf{S}_{\mathrm{CO_2}}$ represents the diagonal measurement error covariance of the original CO_2 observations.

Critical to proper uncertainty quantification is rigorous error propagation accounting for the full error covariance matrix, including off-diagonal spatial correlations. For reconstruction-based methods, these correlations arise from the ratio fitting process and can dominate the integrated emission uncertainty even when pixel-level noise appears reduced. The impact of these correlations on emission uncertainty is quantified in Section 5.

https://doi.org/10.5194/egusphere-2026-1134
Preprint. Discussion started: 9 March 2026

5 Results

We assess the performance of CO_2 emission estimation and chemistry parameter retrieval using the synthetic TANGO observations for four emission scenarios: 2.0, 2.5, 5.0, and 12.5 Mt yr^{-1}, as outlined in Section 3.2. This allows direct comparison between analytical precision calculations and Monte Carlo simulations under realistic TANGO-like noise conditions. Monte Carlo simulations were performed using 10 independent MicroHH plume realizations, with 500 Gaussian noise realizations added to both CO_2 and NO_2, and emission rates computed via the Integrated Mass Enhancement (IME) method. This setup enables evaluation of both the CO_2/NO_2 ratio reconstruction and simpler NO_2-based plume masking approaches in terms of precision, bias, and noise propagation. In addition, the methods are applied to EnMAP satellite observations to demonstrate feasibility and robustness on real-world data.

5.1 Emission Estimation Performance

Table 1 presents comprehensive emission estimation results for both NO_2-based masking and CO_2/NO_2 reconstruction approaches across all four emission strengths under ideal conditions—perfect spatial and temporal co-location. Performance depends strongly on source strength, revealing a clear hierarchy in method applicability.

At the lowest emission strength of 2.0 Mt yr^{-1}, both approaches show substantial limitations. The NO_2 masking approach retrieves 1.22 kmol s^{-1} with a bias of -15.3 % and precision of 18.5 % (Monte Carlo) or 11.8 % (analytical). The reconstruction approach performs worse, retrieving 1.06 kmol s^{-1} with a bias of -26.6 % and precision of 19.0 % (Monte Carlo) or 12.8 % (analytical). These substantial biases reflect persistent ratio fitting errors when the CO_2 signal is weak relative to measurement noise. The insufficient CO_2 signal-to-noise ratio prevents reliable characterization of the ratio evolution, leading to systematic underestimation of the true emission in a non-linear least squares fit. Chemistry parameters at this emission level exhibit uncertainties exceeding 100 % for m_1 and τ_d, rendering them uninterpretable. This emission strength falls below TANGO's operational detection threshold. At 2.5 Mt yr^{-1}, representing TANGO's nominal detection limit, the NO_2 masking approach shows marked improvement: 1.65 kmol s^{-1} retrieved emission with -8.1 % bias and 14.0 % precision (Monte Carlo) or 10.1 % (analytical). In contrast, the reconstruction approach still exhibits substantial bias: 1.41 kmol s^{-1} with -21.4 % bias and 14.6 % precision (Monte Carlo) or 11.1 % (analytical). While both methods achieve similar precision (14–15 %), the masking approach demonstrates superior bias characteristics, making it operationally preferable for weak sources near the detection threshold. Chemistry parameters remain poorly constrained, with m_1 uncertainty at 77.8 % and τ_d uncertainty at 78.3 %, precluding meaningful atmospheric interpretation.

At an emission rate of 5.0 Mt yr^{-1}, both retrieval strategies achieve acceptable performance. The masking method yields an inferred flux of 3.67 kmol s^{-1} with a bias of $+1.9$ % and a precision of 7.6 % (Monte Carlo estimate) or 6.8 % (analytical estimate). The reconstruction method yields 3.44 kmol s^{-1} with a bias of -4.3 % and a precision of 7.3 % (Monte Carlo) or 6.9 % (analytical). For both approaches, the precision is on the order of 7 %, and the biases are reduced to within ± 5 %. This emission level thus marks a critical threshold at which the CO_2 signal becomes sufficiently strong to enable robust characterization of concentration ratios. At this emission magnitude, the inferred chemistry parameters become physically interpretable:

https://doi.org/10.5194/egusphere-2026-1134
Preprint. Discussion started: 9 March 2026

$m_1 = 3799.7$ with a relative precision of 25.7 %, $m_0 = 729.9$ with 14.3 % precision, and $\tau_d = 2011.2$ m with 32.3 % precision. Although the associated uncertainties remain considerable, they are sufficiently constrained to allow qualitative evaluation of the plume chemistry evolution. At the highest emission strength of our study of 12.5 Mt yr^{-1}, both methods achieve robust performance. The masking approach retrieves 9.22 kmol s^{-1} with +2.4 % bias and 3.4 % precision (Monte Carlo) or 3.1 % (analytical). The reconstruction approach retrieves 9.40 kmol s^{-1} with +4.5 % bias and 3.1 % precision (Monte Carlo) or 2.8 % (analytical). Both approaches achieve approximately 3 % emission precision with small biases below 5 %, demonstrating the fundamental method capabilities under optimal signal conditions. Chemistry parameters are well-constrained: $m_1 = 5349.5$ with 7.4 % uncertainty, $m_0 = 904.3$ with 6.2 % uncertainty, and $\tau_d = 2302.9$ m with 9.7 % uncertainty, enabling quantitative characterization of atmospheric chemistry processes. Across all emission strengths, Monte Carlo and analytical uncertainties agree within 1–2 percentage points, validating the linear error propagation framework described in Section 4. The final column of Table 1 shows that fixing chemistry parameters to true values (known from noise-free simulations) reduces emission uncertainty by approximately a factor of two for the 12.5 Mt yr^{-1} case (1.6 % versus 3.1 %), demonstrating best-case performance with perfect prior knowledge—unavailable operationally.

5.2 Method Comparison: Masking versus Reconstruction

Direct comparison between NO_2-based masking and CO_2/NO_2 reconstruction reveals a counter-intuitive central finding: despite producing visually cleaner CO_2 fields with suppressed pixel-scale noise (Figure 2), reconstruction does not improve emission precision relative to simple masking. At low emissions (2.0 and 2.5 Mt yr^{-1}), masking shows superior bias characteristics (-15.3 % and -8.1 %) compared to reconstruction (-26.6 % and -21.4 %). At intermediate and high emissions (5.0 and 12.5 Mt yr^{-1}), both achieve comparable accuracy with biases within ±2–5 %. Precision remains essentially equivalent across all emission strengths: approximately 19 %, 14 %, 7 %, and 3 % for the four cases, respectively. For emission estimates, this precision equivalence despite markedly different noise appearance of the plume requires careful explanation. The reconstruction process fits a three-parameter exponential function to the observed CO_2/NO_2 ratio, which cannot capture high-frequency pixel-scale fluctuations. The uncorrelated CO_2 measurement noise enters the ratio and maps onto the fitted parameters (m_0, m_1, τ_d). When the fitted ratio is multiplied by NO_2 to reconstruct CO_2 (Eq. 12), pixel-scale noise variability is suppressed (first term in Eq. (13)), but spatial correlations of noise spanning the entire plume extent are introduced. The uncorrelated errors due to direct mapping of the NO_2 error (second term in Eq. (13)) is not a dominant error term.

For spatial integration in the IME method, the error correlations dominate total uncertainty because the individual errors on the CO_2 columns coherently add rather than cancel. In contrast, uncorrelated pixel noise in the original CO_2 field (used by the masking approach) averages out during integration, following $\sigma_{\text{total}} \propto \sqrt{N}$ scaling. This behavior applies generically to any method using NO_2 to smooth, regularize, or reconstruct CO_2 fields. A critical implication of this is that such methods must provide complete error covariance matrices to demonstrate genuine error reduction. Computing emission precision neglecting spatial correlations introduced by the fitting or smoothing process, can severely underestimate the precision of the emission estimates. In our reconstruction approach, accounting for the full covariance matrix (off-diagonal terms in $\mathbf{S}_{\text{recon}}$) increases the integrated emission uncertainty by more than a factor of 60 compared to cases ignoring error correlation.

https://doi.org/10.5194/egusphere-2026-1134
Preprint. Discussion started: 9 March 2026

Coming back to the plume masking approach, Figure 4 quantifies the trade-off between emission bias and precision for different masking thresholds for the 12.5 Mt yr^{-1} case. Two masking strategies are compared: applying a threshold to CO_2 observations (blue) versus NO_2 observations (red), with thresholds defined as multiples of the respective noise standard deviations (σ_{CO_2} = 0.576 mol m^{-2}, σ_{NO_2} = 3.75×10^{-5} mol m^{-2}). Without masking (threshold <0), plume mass is unbiased but exhibits the largest random error as the entire background noise is integrated (Figure 4b). Thresholding CO_2 reduces precision but rapidly increases bias: low thresholds preferentially exclude negative noise creating positive bias (Figure 4a), while high thresholds truncate true signal causing negative bias. Figure 4c shows total error defined by $e_{\mathrm{tot}} = \sqrt{\mathrm{b}^2 + \sigma^2}$ with precision σ and bias b. It demonstrates that no single CO_2 threshold achieves robust performance across the full bias-precision trade-off.

Figure 5 illustrates spatial effects of a NO_2 masking strategies for the CO_2 plume mask. The true plume mask (white contour, 0.008 mol m^{-2} threshold from noise-free CO_2) serves as reference. Panel (a) with $CO_2 > 0$ shows isolated noise features inflating integrated mass. Panel (b) with $CO_2 > 1.5\sigma_{CO_2}$ suppresses noise but truncates plume edges. Panel (c) demonstrates NO_2-derived masking: a threshold of $3\sigma_{NO_2}$ yields <1 % bias and approximately 2 % random error, closely following the true plume extent while avoiding both noise contamination and premature truncation. This NO_2-based approach represents approximately a factor-of-two improvement in precision compared to analyzing CO_2 without NO_2 guidance. Thus for TANGO emission quantification, we recommend NO_2-based masking: it is computationally simpler than reconstruction, exhibits superior bias characteristics for weak sources below 5 Mt yr^{-1}, and achieves equivalent precision across all emission strengths. The main value of the reconstruction approach lies in enabling chemistry parameter retrieval, discussed in the following subsection.

5.3 Chemistry Parameter Retrieval

As outlined in Section 4.1, the fit of the model in Eq. (1) to CO_2 and NO_2 observations simultaneously retrieves three chemistry parameters: the spatial decay scale τ_d, the amplitude m_1, and the background ratio m_0, with the apparent source ratio given by $m_1 + m_0$ (Table 1). These parameters describe plume evolution processes, complementing emission estimates. The quality of the retrieved parameters depends critically on emission strength, following the same hierarchy observed for emission quantification. At 2.0 and 2.5 Mt yr^{-1}, chemistry parameters are uninterpretable due to errors exceeding 70–100 %. Weak CO_2 signals provide insufficient information to constrain the ratio evolution. At 5.0 Mt yr^{-1}, parameters become interpretable: $m_1 = 3799.7$ (25.7 % precision), $m_0 = 729.9$ (14.3 % precision), and $\tau_d = 2011.2$ m (32.3 % precision). While uncertainties remain substantial, they permit qualitative assessment of plume chemistry. At 12.5 Mt yr^{-1}, robust retrieval is achieved: $m_1 = 5349.5$ (7.4 % precision), $m_0 = 904.3$ (6.2 % precision), and $\tau_d = 2302.9$ m (9.7 % precision), enabling quantitative characterization. Overall, the interpretation of these parameters even for moderate precisions requires careful consideration of observational constraints and potential biases.

The spatial decay parameter τ_d exhibits the clearest interpretation among the three fitted parameters. Retrieved values of 2100–2300 m for the medium and large emission cases substantially exceed TANGO's 300 m point spread function, indicating that τ_d represents a genuine atmospheric process which is little affected by the forward model error that we discussed in Sec. 4.2. The decay scale characterizes the spatial evolution of the CO_2/NO_2 ratio along the plume: higher values indicate slower ratio changes, while lower values indicate rapid decay. When combined with information on the wind speed U in the plume

https://doi.org/10.5194/egusphere-2026-1134
Preprint. Discussion started: 9 March 2026

direction, τ_d converts to an effective chemical timescale $\tau_s = \tau_d/U$ that quantifies the effective rate of NO $\rightarrow$ NO_2 conversion relative to the conservative tracer CO_2.

In the simulation, the background O_3 concentration is 30 ppb and the rate coefficient for $NO + O_3 \rightarrow NO_2 + O_2$ is $k = 1.9 \times 10^{-14}$ cm^3 molecule^{-1} s^{-1}, giving a theoretical clean-air NO lifetime of $\tau_{\mathrm{chem}} = (k\,[O_3])^{-1} \approx 70$ s. The competing photolysis reaction $NO_2 + h\nu \rightarrow NO + O$ partly counteracts this conversion, with a daytime timescale of ~ 300 s, so the net NO $\rightarrow$ NO_2 conversion in clean air is slower than the 70 s lower limit. In practice, however, the fresh plume rapidly titrates local O_3, reducing its concentration and substantially lengthening the effective conversion timescale. The degree of this ozone depletion is controlled by turbulent mixing: faster dilution replenishes background O_3 more quickly, shortening τ_s, while slower dilution sustains O_3 depletion and extends it. The retrieved τ_s therefore encodes both chemistry and plume dynamics. For the simulation, the imposed boundary wind is 5 m s^{-1}, but surface friction reduces the effective mass-weighted wind speed within the plume to approximately 4 m s^{-1}, yielding $\tau_s = \tau_d/U \approx 2300\,\mathrm{m}/4\,\mathrm{m\,s^{-1}} \approx 575$ s.

The apparent source ratio $m_1 + m_0$ nominally represents the CO_2/NO_2 ratio extrapolated back to the emission source location. For the 12.5 Mt yr^{-1} case, the retrieved value is $m_1 + m_0 = 5349.5 + 904.3 = 6253.8$. In principle, this could reveal information about combustion characteristics, fuel composition, or emission control technologies. However, this parameter is biased by more than 25 % at TANGO's 300 m spatial resolution, preventing direct interpretation as the true emission ratio without careful correction. This bias arises from the limited spatial resolution of satellite instruments, which cannot fully resolve the narrow plumes near the source. Where the ratio model describes the ratio of 'real' fields, the observed ratio is affected by the instrument spatial response that blurs the observed CO_2 and NO_2 field independently. This affects the accuracy of the retrieved quantity $m_1 + m_0$ which is mainly determined at the source location of the plume. Consequently, $m_1 + m_0$ cannot be directly interpreted as the true CO_2/NO_2 emission ratio without accounting for these resolution-dependent biases.

Finally, we discuss the background ratio m_0, which represents the CO_2/NO_2 ratio in the far downwind portion of the plume, where atmospheric processing has progressed to an approximate NO_x equilibrium. Retrieved m_0 values range from approximately 730 to 900 for the larger emission cases (Table 1). Given its definition, one might wish to use m_0 to infer the true background CO_2/NO_x emission ratio. However, any conversion of m_0 to this underlying emission ratio depends on atmospheric parameters that are not directly constrained by the TANGO observations, such as the degree of O_3 depletion within the plume. Despite this limitation in interpretability, m_0 remains valuable as an empirical diagnostic: it represents the NO_2/CO_2 ratio far downwind where the plume has diluted sufficiently for background air to dominate, restoring the ambient NO_2/CO_2 ratio. Systematic variations in m_0 across different locations or atmospheric regimes can therefore provide insight into differences in background composition and plume-chemistry evolution, even if its absolute value cannot be unambiguously related to intrinsic emission characteristics. Within the plume lengths analysed here (<15 km), NO_x oxidation via $NO_2 + OH$ (lifetime $\sim$2 h) is a secondary effect; however, its influence is implicitly absorbed into the fitted parameters, in particular m_0, which encodes the far-field CO_2/NO_2 ratio where such processing has already modified the NO_2/NO_x partitioning.

https://doi.org/10.5194/egusphere-2026-1134
Preprint. Discussion started: 9 March 2026

5.4 Robustness to Spatial and Temporal Misalignment

Up to this point, the CO_2–NO_2 synergy has been analyzed under the idealized assumption of perfectly aligned observations of both species. For TANGO, however, due to the configuration comprising the two CubeSats TANGO-Carbon and TANGO-Nitro, the CO_2 and NO_2 measurements are neither spatially nor temporally fully co-located. To assess the robustness of our methodology under realistic TANGO operational conditions, we again consider the 12.5 $\mathrm{Mt\,yr^{-1}}$ base case and conduct an extensive Monte Carlo experiment: 10 independent MicroHH plume snapshots are each combined with 500 distinct noise realizations, resulting in 5000 total realizations per configuration. Both the masking and reconstruction strategies are then evaluated for their sensitivity to spatial and temporal misalignment between the CO_2 and NO_2 observations, simulated by sampling CO_2 and NO_2 on shifted grids and by selecting plume snapshots with varying time separations.

5.4.1 Spatial grid misalignment

Figure 6 examines the effect of spatial misalignment between the CO_2 and NO_2 observation grids. The NO_2 grid is shifted systematically in both x and y directions by distances up to 150 m (half a TANGO pixel), and emission estimates are computed for both masking and reconstruction approaches. Blue symbols show emissions estimated from CO_2 only (independent of grid shift), orange symbols show emissions from reconstructed CO_2 using NO_2 measurements. Error bars indicate the standard deviation across noise realizations, while dotted lines denote analytically derived error estimates. Both methods show excellent stability: emission biases remain below 2 % for grid shifts up to 150 m. Monte Carlo and analytical uncertainties closely match across all tested offsets, confirming that the error propagation framework correctly accounts for spatial misalignment effects. Chemistry parameters retrieved via reconstruction are similarly robust: $m_1 + m_0$, m_0, and τ_d fluctuate by less than 5 %, well within their 7–10 % retrieval uncertainties. Thus, spatial grid alignment is not a critical error source for TANGO, even for misalignments up to half a pixel.

5.4.2 Temporal separation

Figure 7 quantifies the effect of temporal offset between CO_2 and NO_2 measurements. The MicroHH simulation provides plume snapshots at 1-minute intervals, enabling evaluation of how time delays between the two satellite observations affect the data interpretation. CO_2 and NO_2 fields are sampled from different time steps to simulate temporal offsets from 0 to 9 minutes, with emissions and chemistry parameters computed for both approaches.

At TANGO's nominal 60 s separation, both approaches exhibit emission biases below 2 %. The masking approach maintains this performance to approximately 2 minutes, with biases increasing gradually beyond this point. The reconstruction approach shows similar robustness up to 2–3 minutes (bias $<$6 %), with substantial deviations only beyond 4 minutes (28 % bias at 6 minutes). These degradations at long temporal separations reflect turbulent transport breaking the simultaneity assumption: turbulent plume structures evolve on timescales of several minutes, and when CO_2 and NO_2 observations sample substantially different plume realizations, the ratio-based reconstruction introduces systematic errors. Note that this sensitivity is expected to be lower under neutral or stable atmospheric conditions, where plume structures evolve more slowly. Chemistry parameters

https://doi.org/10.5194/egusphere-2026-1134
Preprint. Discussion started: 9 March 2026

exhibit greater temporal sensitivity than emissions. Below 60 s, turbulent structures in CO_2 and NO_2 remain sufficiently correlated that they produce smooth CO_2/NO_2 evolution: $m_1 + m_0$ varies by less than 3 %, m_0 by less than 5 %, and τ_d by less than 8 %. Beyond 2 minutes, different plume representations introduce ratio fluctuations unrelated to chemistry. Retrieved τ_d systematically increases with temporal offset, reflecting artificial ratio evolution from spatial mismatch between the two plumes. Analytical uncertainties deviate from Monte Carlo values beyond 3 minutes, indicating that the linear error model assumptions fail at these long separations. Chemistry retrieval therefore requires tighter temporal co-location than emission quantification, with 60 s representing a practical upper limit for reliable parameter characterization. For emissions alone, temporal separations up to 2–3 minutes remain acceptable.

Across all tests, analytical error propagation agrees excellently with Monte Carlo simulations under nominal TANGO conditions (60 s temporal, 150 m spatial), validating the error models for operational uncertainty quantification. Primary limitations arise from signal-to-noise constraints at low emissions rather than co-location inaccuracies. Neither 60 s temporal separation nor 150 m spatial misalignment constitutes a dominant error source, confirming reliable performance under realistic mission conditions. Quantitatively, spatial offsets from 0 to 150 m produce emission variations below 0.5 % for both methods, while temporal separations from 0 to 60 s produce variations below 1 %. Even at 3 minutes temporal offset, emission biases remain below 8 %, demonstrating substantial margin beyond TANGO's 60 s operational requirement. These robustness margins confirm that neither spatial interpolation accuracy nor temporal co-registration represents a limiting factor for TANGO emission quantification.

5.5 Application to EnMAP Observations

We demonstrate the method on real satellite data using EnMAP observations over three industrial sources from Borger et al. (2025): Matla (5 October 2023), and two power plants close to Riyadh (PP10, 11 July 2023 and PP9, 15 July 2023). EnMAP provides hyperspectral measurements at 30 m spatial resolution, enabling simultaneous CO_2 and NO_2 retrievals from the same overpass. Both retrievals exhibit artifacts such as along-track stripes and surface-related patterns from radiometric calibration uncertainties and spectral interference, more pronounced in CO_2 than NO_2. Site characteristics, observation dates, and wind conditions are summarized in Table 2. Wind speeds vary from 2.79 m s^{-1} (Matla) to 8.76 m s^{-1} (PP9), affecting plume dispersion and NO_2 plume evolution in downwind direction. Because Borger et al. (2025) did not provide retrieval error estimates, we estimated measurement noise from the standard deviation of non-plume background pixels in each scene: 0.65 mol m^{-2} for CO_2 and 2.92×10^{-4} mol m^{-2} for NO_2 at Matla, with similar values for the other sites. However, Borger et al. (2025) applied destriping and smoothing prior to emission quantification. Consequently, these noise estimates are likely too low, and the assumption of uncorrelated pixel-to-pixel errors is likely invalid. The true error structure is dominated by spatially correlated residuals from preprocessing, which cannot be reliably characterized from background variability alone.

Figure 8 shows application of both masking and reconstruction approaches to the three sites. Row (a–c) displays original EnMAP CO_2 retrievals with clear plume structures but substantial noise and surface artifacts. Row (d–f) shows reconstructed CO_2 fields after CO_2/NO_2 reconstruction, exhibiting smoother plumes with reduced interference. Row (g–i) shows NO_2 retrievals with lower noise but some remaining artifacts. Row (j–l) displays differences between original and reconstructed CO_2

https://doi.org/10.5194/egusphere-2026-1134
Preprint. Discussion started: 9 March 2026

fields, highlighting noise and bias reduction achieved through the ratio-based approach. As demonstrated earlier, however, this visual noise reduction does not translate into a reduced error on the retrieved emission flux compared to using the original CO_2 field directly. Table 3 compares emission estimates and retrieved reconstruction parameters across the three sites. We note that Borger et al. (2025) used the cross-sectional flux method and reported maximum values within 10 km from the source, methodologically different from our integrated mass enhancement (IME) method. We averaged their cross-sectional flux estimates over the 10 km downwind range to obtain representative values more comparable to spatially integrated IME results.

For Matla and PP10, emissions from CO_2 measurements with NO_2 masking (26.9 Mt yr^{-1} and 47.4 Mt yr^{-1}) and reconstructed fields (25.3 Mt yr^{-1} and 45.2 Mt yr^{-1}) agree well with averaged published values (28.1 Mt yr^{-1} and 46.0 Mt yr^{-1}). For PP9, CO_2 with NO_2 masking yields 55.6 Mt yr^{-1} and the reconstructed field gives 49.6 Mt yr^{-1}, both consistent with the averaged published value of 52.6 Mt yr^{-1}. These results demonstrate that both masking and ratio-based reconstruction are applicable to real EnMAP measurements, successfully reproducing previously published emission estimates. Retrieved reconstruction parameters provide additional insight into plume chemistry and atmospheric conditions. The apparent CO_2/NO_2 source ratio ($m_1 + m_0$) is highest for Matla (3391), while the two Riyadh power plants exhibit similar values (PP10: 2410, PP9: 2834). These differences may reflect variations in combustion efficiency, fuel composition, or flue gas treatment, though they must be interpreted cautiously due to the resolution-dependent biases discussed in Section 5 (bias $>25\,\%$ expected at finite spatial resolution).

The spatial decay parameter τ_d shows substantial variation: Matla exhibits 1744 m, PP10 shows 3188 m, and PP9 displays 1451 m. When converted to temporal scales using observed wind speeds (Table 2), PP9 exhibits the fastest effective chemical timescale ($\tau_s = \tau_d/U = 166$ s), whereas for Matla and PP10, τ_s values are similar with $\tau_s = 626$ s and 744 s, respectively. The faster evolution of the CO_2/NO_2 ratio, indicates different chemical boundaries for the PP9 plume compared to the other two plumes. The background ratio m_0 also varies across sites. Again, Matla and PP10 show similar results with $m_0 = 1007$ and 941, respectively, whereas PP9 deviates from this with $m_0 = 1274$. This supports our conclusion based on τ_s, although we are aware that a more detailed chemical analysis is required to interpret the results. The large spread in τ_s across sites (166–744 s) likely reflects differences in boundary-layer turbulence intensity: stronger turbulence entrains background O_3 into the plume more rapidly, shortening the effective $NO \rightarrow NO_2$ timescale. The notably short τ_s at PP9 (166 s, close to the clean-air theoretical minimum of $\sim$70 s) is consistent with its high wind speed and vigorous mixing, whereas the longer timescales at Matla and PP10 suggest more sustained O_3 depletion under calmer conditions. Boundary-layer turbulence diagnostics from atmospheric reanalysis products (e.g., CAMS) could be used to test this interpretation quantitatively, but this is beyond the scope of the present study. These results from EnMAP suggest that all the chemistry parameters retrieved from the data remain interpretable even in real EnMAP observations when combined with ancillary wind information, despite complexities from finite spatial resolution and retrieval artifacts.

Quantitative error estimation in EnMAP data is severely limited by preprocessing applied to the products provided by Borger et al. (2025). Input noise estimates from background pixels likely underestimate true uncertainties due to smoothing and destriping that introduce spatial correlations. Consequently, our analytically propagated errors (0.04–0.06 kmol s^{-1}, or

https://doi.org/10.5194/egusphere-2026-1134
Preprint. Discussion started: 9 March 2026

approximately 0.1 % relative uncertainty) appear unrealistically small compared to published uncertainties from Borger et al. (2025) (6.38–14.64 kmol s^{-1}, or approximately 20–30 % relative uncertainty). Our tabulated uncertainties should be regarded as lower bounds reflecting only propagated measurement noise under assumptions of perfect functional form and error-free ancillary data, not accounting for systematic errors, model limitations, or preprocessing-induced correlations.

A clear limitation is that reconstruction assumes NO_2 measurements are free of artifacts. Any spurious features in NO_2—such as striping or calibration errors—are directly imprinted onto reconstructed CO_2 fields through the ratio multiplication (Eq. 12), making reconstruction accuracy highly sensitive to NO_2 data quality. This is evident in Figure 8, particularly panel (i), where remaining NO_2 artifacts propagate into the reconstructed CO_2 field. Nonetheless, successful application to EnMAP observations demonstrates practical feasibility of the CO_2/NO_2 synergy approach on real satellite data. Emission estimates agree with independent published results, and chemistry parameters exhibit physically reasonable values with systematic site-to-site variations. For TANGO, with optimized instrument design, consistent measurement characteristics, lower noise levels, and availability of full retrieval error covariances, we expect more robust performance and reliable uncertainty quantification when complete error propagation is applied. The method is ready for deployment in TANGO and other multi-species satellite missions including GOSAT-GW and CO2M.

6 Conclusions

We present a CO_2–NO_2 synergy method for the TANGO mission and similar satellite platforms providing co-located observations of both species, including EnMAP, GOSAT-GW, and CO2M, and demonstrate its performance on both large-eddy simulations and real EnMAP observations. The method addresses a fundamental challenge in high-resolution greenhouse gas monitoring: Measured CO_2 plume enhancements suffer from substantial measurement noise, whereas NO_2 observations exhibit much higher signal-to-noise ratios over the same industrial facilities. The primary value of NO_2 synergy lies in plume detection and masking. By using NO_2 observations to define spatial masks identifying plume extent, then integrating CO_2 within these masks, emission precision improves by approximately a factor of two relative to analyzing CO_2 without NO_2 guidance. Across emission strengths of 2.0, 2.5, 5.0, and 12.5 Mt yr^{-1}, the masking approach achieves total emission precision of 18.5 %, 14.0 %, 7.6 %, and 3.4 %, respectively, under TANGO-like conditions. Critically, masking exhibits superior bias characteristics for weak sources: at the TANGO detection limit of 2.5 Mt yr^{-1}, masking shows -8.1 % bias. Below 2.5 Mt yr^{-1}, both approaches show substantial biases exceeding 15 %, in agreement with the reported operational detection limit Landgraf and Veefkind (2025).

Our second approach—CO_2/NO_2 ratio reconstruction—fits an exponential model to the observed ratio and generates smoothed CO_2 fields. Despite producing visually cleaner fields with reduced pixel-scale noise, reconstruction does not improve emission precision relative to masking. This counter-intuitive finding has a fundamental explanation: reconstruction transforms uncorrelated pixel noise into spatially correlated errors affecting larger plume areas coherently. When integrating across the entire plume, these correlated errors dominate the error propagation, offsetting any benefit from reduced pixel-scale noise. We demonstrate that neglecting spatial error correlations—using only diagonal covariance matrix elements—underestimates true emis-

https://doi.org/10.5194/egusphere-2026-1134
Preprint. Discussion started: 9 March 2026

sion uncertainties by factors exceeding 60. This finding applies generically to any method combining CO_2 and NO_2 through smoothing, regularization, or reconstruction: studies claiming emission uncertainty reduction through synergistic multi-species approaches must provide complete error covariance matrices to prove genuine precision improvement rather than merely redistributing errors across spatial scales. Both masking and reconstruction remain robust to realistic TANGO operational constraints. Spatial grid misalignments up to 150 m introduce biases below 2 %. Temporal separations up to 60 s produce emission biases below 2 %, and emission estimates remain acceptable for temporal offsets up to 2–3 minutes.

While reconstruction does not reduce emission uncertainty, its primary value lies in atmospheric chemistry characterization. The method retrieves three parameters describing plume chemical evolution: the spatial decay scale τ_d, the apparent source ratio $m_1 + m_0$, and the background ratio m_0. The spatial decay parameter exhibits the clearest physical interpretation: retrieved values of 2100–2300 m substantially exceed TANGO's 300 m instrumental resolution, confirming representation of genuine atmospheric processes. When divided by wind speed, τ_d converts to an effective chemical timescale τ_s characterizing $NO \rightarrow NO_2$ oxidation rates, providing a direct observation-based measure of plume chemistry comparable across facilities and atmospheric conditions. The apparent source ratio $m_1 + m_0$ is biased by more than 25 % at TANGO's 300 m resolution because CO_2 and NO_2 form plumes with different spatial structures near the source. The background ratio m_0 should only be interpreted as a CO_2/NO_2 ratio and an extension to a more useful CO_2/NO_x ratio remains difficult. Despite these interpretational constraints, all three parameters can provide useful information on the NO_x chemistry within an emission plume and exhibit systematic behavior across emission strengths and atmospheric conditions. The quality of the chemistry parameter depends critically on emission strength. Using simulated TANGO observations for CO_2 emissions of 2.0 and 2.5 Mt yr^{-1}, parameters show uncertainties exceeding 70 %, precluding interpretation. At 5.0 Mt yr^{-1}, parameters become interpretable with 15–30 % uncertainties. At 12.5 Mt yr^{-1}, robust retrieval is achieved with 6–10 % uncertainties, enabling quantitative chemistry characterization.

Application to three EnMAP satellite observations demonstrates real-world feasibility. Emission estimates from both masking and reconstruction agree well with previously published values, and retrieved chemistry parameters exhibit physically reasonable values with systematic site-to-site variations. The effective chemical timescale of the $NO \rightarrow NO_2$ conversion is in the range 166–744 s, confirming physically meaningful characterization. Quantitative error assessment is limited by preprocessing applied to EnMAP products, but successful application confirms operational readiness.

By observing more than 10,000 facilities annually, TANGO will give us the opportunity to build an unprecedented database of site-specific chemistry parameters spanning diverse emission sources and atmospheric conditions. This database could support more robust emission analyses through empirical chemistry constraints, improve NO_x emission estimates from NO_2-only missions, and enable machine learning models predicting chemistry parameters from meteorology and source characteristics. Furthermore, the derived chemistry parameters can be systematically applied to NO_2 retrievals from missions lacking CO_2 observations, enabling indirect CO_2 emission estimates through empirically-constrained relationships between NO_2 and CO_2 sources. For operational emission estimates from TANGO CO_2 and NO_2 observations, we recommend NO_2-based plume masking approach for CO_2 emission quantifications with computational simplicity, superior bias characteristics for weak sources, and straightforward uncertainty propagation. This work highlights the importance of rigorous uncertainty quantifi-

https://doi.org/10.5194/egusphere-2026-1134
Preprint. Discussion started: 9 March 2026

cation in multi-species synergy methods: a complete error covariance matrix accounting for spatial correlations is needed to demonstrate whether a given approach achieves genuine precision improvement in emission estimates. The CO_2–NO_2 synergy approach is validated, robust to operational constraints, and ready for TANGO deployment.

Data availability. The MicroHH simulation dataset generated in the context of this study will be provided in the final version of the manuscript.

Author contributions. T.B. conceived the study, developed the CO_2–NO_2 plume reconstruction method, performed the analysis, and wrote the manuscript. M.K. conducted the MicroHH large-eddy simulations and contributed to the interpretation of atmospheric chemistry processes. P.V. provided expertise on the TANGO mission design and observational requirements. J.L. initiated and supervised the study and contributed to the methodological framework. All authors contributed to the discussion of results and revision of the manuscript.

Competing interests. The authors declare that they have no conflict of interest.

Acknowledgements. We acknowledge the European Space Agency (ESA) for supporting the TANGO mission development under the SCOUT programme. We thank the MicroHH development team for providing the large-eddy simulation framework. We are grateful to the EnMAP mission team for making satellite observations publicly available. This research was carried out at SRON Space Research Organization Netherlands with support from the Netherlands Space Office (NSO).

https://doi.org/10.5194/egusphere-2026-1134
Preprint. Discussion started: 9 March 2026

References

Beirle, S., Borger, C., Dörner, S., Li, A., Hu, Z., Liu, F., Wang, Y., and Wagner, T.: Pinpointing nitrogen oxide emissions from space, Science Advances, 5, eaax9800, https://doi.org/10.1126/sciadv.aax9800, 2019.

Borger, C., Beirle, S., Butz, A., Scheidweiler, L. O., and Wagner, T.: High-resolution observations of NO2 and CO2 emission plumes from EnMAP satellite measurements, Environmental Research Letters, 20, 044 034, https://doi.org/10.1088/1748-9326/adc0b1, 2025.

Borsdorff, T., Hasekamp, O. P., Wassmann, A., and Landgraf, J.: Insights into Tikhonov regularization: application to trace gas column retrieval and the efficient calculation of total column averaging kernels, Atmospheric Measurement Techniques, 7, 523–535, https://doi.org/10.5194/amt-7-523-2014, 2014.

Brenny, B., Day, J., de Goeij, B., Palombo, E., Ouwerkerk, B., Koc, N. A., Bell, A., Leemhuis, A., Paskeviciute, A., Buisset, C., and Malavart, A.: Development of spectrometers for the TANGO greenhouse gas monitoring missions, in: International Conference on Space Optics — ICSO 2022, edited by Minoglou, K., Karafolas, N., and Cugny, B., vol. 12777, p. 127771S, International Society for Optics and Photonics, SPIE, https://doi.org/10.1117/12.2689936, 2023.

Charuvil Asokan, H., Landgraf, J., Veefkind, P., Dellaert, S., and Butz, A.: Assessing the detection potential of targeting satellites for global greenhouse gas monitoring: insights from TANGO orbit simulations, Atmospheric Measurement Techniques, 18, 5247–5264, https://doi.org/10.5194/amt-18-5247-2025, 2025.

Day, J., Brenny, B., Palombo, E., de Goeij, B., Ouwerkerk, B., Misiun, G., Lemmen, M., Koc, N. A., Leemhuis, A., Landgraf, J., Sivil, D., Michel, B., Paskeviciute, A., Buisset, C., Windpassinger, R., and Malavart, A.: Development of the TANGO carbon instrument for greenhouse gas detection, in: Remote Sensing Technologies and Applications in Urban Environments VIII, edited by Erbertseder, T., Chrysoulakis, N., and Zhang, Y., vol. 12735, p. 127350I, International Society for Optics and Photonics, SPIE, https://doi.org/10.1117/12.2680270, 2023.

Fioletov, V., McLinden, C. A., Griffin, D., Zhao, X., and Eskes, H.: Global seasonal urban, industrial, and background NO_2 estimated from TROPOMI satellite observations, Atmospheric Chemistry and Physics, 25, 575–596, https://doi.org/10.5194/acp-25-575-2025, 2025.

Friedlingstein, P., O'Sullivan, M., Jones, M. W., Andrew, R. M., Gregor, L., Hauck, J., Le Quéré, C., Luijkx, I. T., Olsen, A., Peters, G. P., Peters, W., Pongratz, J., Schwingshackl, C., Sitch, S., Canadell, J. G., Ciais, P., Jackson, R. B., Alin, S. R., Alkama, R., Arneth, A., Arora, V. K., Bates, N. R., Becker, M., Bellouin, N., Bittig, H. C., Bopp, L., Chevallier, F., Chini, L. P., Cronin, M., Evans, W., Falk, S., Feely, R. A., Gasser, T., Gehlen, M., Gkritzalis, T., Gloege, L., Grassi, G., Gruber, N., Gürses, O., Harris, I., Hefner, M., Houghton, R. A., Hurtt, G. C., Iida, Y., Ilyina, T., Jain, A. K., Jersild, A., Kadono, K., Kato, E., Kennedy, D., Klein Goldewijk, K., Knauer, J., Korsbakken, J. I., Landschützer, P., Lefèvre, N., Lindsay, K., Liu, J., Liu, Z., Marland, G., Mayot, N., McGrath, M. J., Metzl, N., Monacci, N. M., Munro, D. R., Nakaoka, S.-I., Niwa, Y., O'Brien, K., Ono, T., Palmer, P. I., Pan, N., Pierrot, D., Pocock, K., Poulter, B., Resplandy, L., Robertson, E., Rödenbeck, C., Rodriguez, C., Rosan, T. M., Schwinger, J., Séférian, R., Shutler, J. D., Skjelvan, I., Steinhoff, T., Sun, Q., Sutton, A. J., Sweeney, C., Takao, S., Tanhua, T., Tans, P. P., Tian, X., Tian, H., Tilbrook, B., Tsujino, H., Tubiello, F., van der Werf, G. R., Walker, A. P., Wanninkhof, R., Whitehead, C., Willstrand Wranne, A., Wright, R., Yuan, W., Yue, C., Yue, X., Zaehle, S., Zeng, J., and Zheng, B.: Global Carbon Budget 2022, Earth System Science Data, 14, 4811–4900, https://doi.org/10.5194/essd-14-4811-2022, 2022.

Hakkarainen, J., Ialongo, I., Oda, T., Szeląg, M. E., O'Dell, C. W., Eldering, A., and Crisp, D.: Building a bridge: characterizing major anthropogenic point sources in the South African Highveld region using OCO-3 carbon dioxide snapshot area maps and Sentinel-5P/TROPOMI nitrogen dioxide columns, Environmental Research Letters, 18, 035 003, https://doi.org/10.1088/1748-9326/acb837, 2023.

Hansen, P. C.: Discrete Inverse Problems, Society for Industrial and Applied Mathematics, https://doi.org/10.1137/1.9780898718836, 2010.

https://doi.org/10.5194/egusphere-2026-1134
Preprint. Discussion started: 9 March 2026

Koene, E. F. M., Kuhlmann, G., and Brunner, D.: Bayesian denoising of satellite images using co-registered NO_2 images, EGUsphere, 2025, 1–27, https://doi.org/10.5194/egusphere-2025-4477, 2025.

Krol, M., van Stratum, B., Anglou, I., and Boersma, K. F.: Evaluating NO_x stack plume emissions using a high-resolution atmospheric chemistry model and satellite-derived NO_2 columns, Atmospheric Chemistry and Physics, 24, 8243–8262, https://doi.org/10.5194/acp-24-8243-2024, 2024.

Kuhlmann, G., Broquet, G., Marshall, J., Clément, V., Löscher, A., Meijer, Y., and Brunner, D.: Detectability of CO_2 emission plumes of cities and power plants with the Copernicus Anthropogenic CO_2 Monitoring (CO2M) mission, Atmospheric Measurement Techniques, 12, 6695–6719, https://doi.org/10.5194/amt-12-6695-2019, 2019.

Kuhlmann, G., Henne, S., Meijer, Y., and Brunner, D.: Quantifying CO2 Emissions of Power Plants With CO2 and NO2 Imaging Satellites, Frontiers in Remote Sensing, Volume 2 - 2021, https://doi.org/10.3389/frsen.2021.689838, 2021.

Landgraf, J. and Veefkind, P.: TANGO Mission Requirement Document, ISISPACE, The Netherlands, issue 2.1, ISIS-TMI-REQ-0001, 2025.

Lee, H. and Romero, J., eds.: Climate Change 2023: Synthesis Report. Contribution of Working Groups I, II and III to the Sixth Assessment Report of the Intergovernmental Panel on Climate Change, Cambridge University Press, Geneva, Switzerland, https://doi.org/10.59327/IPCC/AR6-9789291691647, 2023.

Li, H., Qiu, J., and Zheng, B.: Air-pollution-satellite-based CO_2 emission inversion: system evaluation, sensitivity analysis, and future research direction, Atmospheric Chemistry and Physics, 25, 1949–1963, https://doi.org/10.5194/acp-25-1949-2025, 2025.

Lorente, A., Boersma, K. F., Eskes, H. J., Veefkind, J. P., van Geffen, J. H. G. M., de Zeeuw, M. B., Denier van der Gon, H. A. C., Beirle, S., and Krol, M. C.: Quantification of nitrogen oxides emissions from build-up of pollution over Paris with TROPOMI, Scientific Reports, 9, 20 033, https://doi.org/10.1038/s41598-019-56428-5, 2019.

Meier, S., Koene, E. F. M., Krol, M., Brunner, D., Damm, A., and Kuhlmann, G.: A lightweight NO_2-to-NO_x conversion model for quantifying NO_x emissions of point sources from NO_2 satellite observations, Atmospheric Chemistry and Physics, 24, 7667–7686, https://doi.org/10.5194/acp-24-7667-2024, 2024.

Moeini, O., Nassar, R., Mastrogiacomo, J.-P., Dawson, M., O'Dell, C. W., Nelson, R. R., and Chatterjee, A.: Quantifying CO2 Emissions From Smaller Anthropogenic Point Sources Using OCO-2 Target and OCO-3 Snapshot Area Mapping Mode Observations, Journal of Geophysical Research: Atmospheres, 130, e2024JD042 333, https://doi.org/https://doi.org/10.1029/2024JD042333, e2024JD042333 2024JD042333, 2025.

Mols, A., Boersma, K. F., Denier van der Gon, H., and Krol, M.: An improved Bayesian inversion to estimate daily NO_x emissions of Paris from TROPOMI NO_2 observations between 2018–2023, Atmospheric Chemistry and Physics, 26, 1497–1513, https://doi.org/10.5194/acp-26-1497-2026, 2026.

Nassar, R., Mastrogiacomo, J.-P., Bateman-Hemphill, W., McCracken, C., MacDonald, C. G., Hill, T., O'Dell, C. W., Kiel, M., and Crisp, D.: Advances in quantifying power plant CO2 emissions with OCO-2, Remote Sensing of Environment, 264, 112 579, https://doi.org/https://doi.org/10.1016/j.rse.2021.112579, 2021.

Nassar, R., Moeini, O., Mastrogiacomo, J.-P., O'Dell, C. W., Nelson, R. R., Kiel, M., Chatterjee, A., Eldering, A., and Crisp, D.: Tracking CO2 emission reductions from space: A case study at Europe's largest fossil fuel power plant, Frontiers in Remote Sensing, Volume 3 - 2022, https://doi.org/10.3389/frsen.2022.1028240, 2022.

Reuter, M., Buchwitz, M., Schneising, O., Krautwurst, S., O'Dell, C. W., Richter, A., Bovensmann, H., and Burrows, J. P.: Towards monitoring localized CO_2 emissions from space: co-located regional CO_2 and NO_2 enhancements observed by the OCO-2 and S5P satellites, Atmospheric Chemistry and Physics, 19, 9371–9383, https://doi.org/10.5194/acp-19-9371-2019, 2019.

https://doi.org/10.5194/egusphere-2026-1134
Preprint. Discussion started: 9 March 2026

Rodgers, C. D.: Inverse Methods for Atmospheric Sounding, WORLD SCIENTIFIC, https://doi.org/10.1142/3171, 2000.

Santaren, D., Hakkarainen, J., Kuhlmann, G., Koene, E., Chevallier, F., Ialongo, I., Lindqvist, H., Nurmela, J., Tamminen, J., Amorós, L., Brunner, D., and Broquet, G.: Benchmarking data-driven inversion methods for the estimation of local CO_2 emissions from synthetic satellite images of XCO_2 and NO_2, Atmospheric Measurement Techniques, 18, 211–239, https://doi.org/10.5194/amt-18-211-2025, 2025.

Tanimoto, H., Matsunaga, T., Someya, Y., Fujinawa, T., Ohyama, H., Morino, I., Yashiro, H., Sugita, T., Inomata, S., Müller, A., Saeki, T., Yoshida, Y., Niwa, Y., Saito, M., Noda, H., Yamashita, Y., Ikeda, K., Saigusa, N., Machida, T., Frey, M. M., Lim, H., Srivastava, P., Jin, Y., Shimizu, A., Nishizawa, T., Kanaya, Y., Sekiya, T., Patra, P., Takigawa, M., Bisht, J., Kasai, Y., and Sato, T. O.: The greenhouse gas observation mission with Global Observing SATellite for Greenhouse gases and Water cycle (GOSAT-GW): objectives, conceptual framework and scientific contributions, Progress in Earth and Planetary Science, 12, 8, https://doi.org/10.1186/s40645-025-00684-9, 2025.

van Geffen, J., Eskes, H., Compernolle, S., Pinardi, G., Verhoelst, T., Lambert, J.-C., Sneep, M., ter Linden, M., Ludewig, A., Boersma, K. F., and Veefkind, J. P.: Sentinel-5P TROPOMI NO_2 retrieval: impact of version v2.2 improvements and comparisons with OMI and ground-based data, Atmospheric Measurement Techniques, 15, 2037–2060, https://doi.org/10.5194/amt-15-2037-2022, 2022.

van Heerwaarden, C. C., van Stratum, B. J. H., Heus, T., Gibbs, J. A., Fedorovich, E., and Mellado, J. P.: MicroHH 1.0: a computational fluid dynamics code for direct numerical simulation and large-eddy simulation of atmospheric boundary layer flows, Geoscientific Model Development, 10, 3145–3165, https://doi.org/10.5194/gmd-10-3145-2017, 2017.

Varon, D. J., Jacob, D. J., McKeever, J., Jervis, D., Durak, B. O. A., Xia, Y., and Huang, Y.: Quantifying methane point sources from fine-scale satellite observations of atmospheric methane plumes, Atmospheric Measurement Techniques, 11, 5673–5686, https://doi.org/10.5194/amt-11-5673-2018, 2018.

Veefkind, J. P., Aben, I., McMullan, K., Forster, H., de Vries, J., Otter, G., Claas, J., Eskes, H. J., de Haan, J. F., Kleipool, Q., van Weele, M., Hasekamp, O., Hoogeveen, R., Landgraf, J., Snel, R., Tol, P. J. J., Ingmann, P., Voors, R., Kruizinga, B., Vink, R., Visser, H. C., and Levelt, P. F.: TROPOMI on the ESA Sentinel-5 Precursor: A GMES mission for global observations of the atmospheric composition for climate, air quality and ozone layer applications, Remote Sensing of Environment, 120, 70–83, https://doi.org/10.1016/j.rse.2011.09.027, 2012.

Zhang, Q., Boersma, K. F., Zhao, B., Eskes, H., Chen, C., Zheng, H., and Zhang, X.: Quantifying daily NO_x and CO_2 emissions from Wuhan using satellite observations from TROPOMI and OCO-2, Atmospheric Chemistry and Physics, 23, 551–563, https://doi.org/10.5194/acp-23-551-2023, 2023.

https://doi.org/10.5194/egusphere-2026-1134
Preprint. Discussion started: 9 March 2026

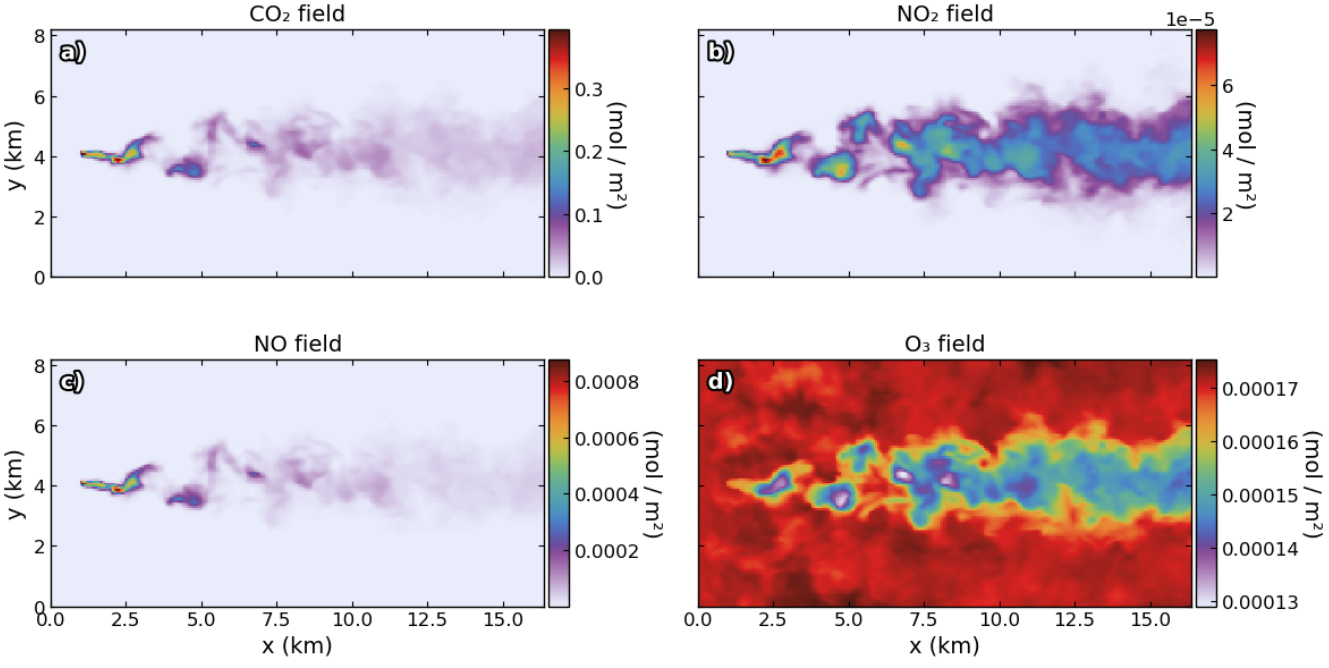

Figure 1. MicroHH large-eddy simulation of a coal-fired power plant plume at 64 m resolution for the 9 kmol s^{-1} (12.5 Mt yr^{-1}) CO_2 emission case. The source (located at $(x_0, y_0, z_0) = (1024, 4096, 200)$ m) emits 9.0 kmol s^{-1} (12.5 Mt yr^{-1}) CO_2, 0.0203 kmol s^{-1} NO, and 0.00107 kmol s^{-1} NO_2 into a 5 m s^{-1} west-to-east wind field with 30 ppb background O_3. Column densities show: (a) CO_2 with maximum enhancement at the source, (b) NO_2 with maximum several kilometers downwind due to photochemical conversion from NO, (c) NO peaking at the source, and (d) O_3 depletion along the plume from NO titration. The spatial offset between CO_2 and NO_2 maxima demonstrates the coupled turbulent-chemical processes captured by the simulation.

https://doi.org/10.5194/egusphere-2026-1134
Preprint. Discussion started: 9 March 2026

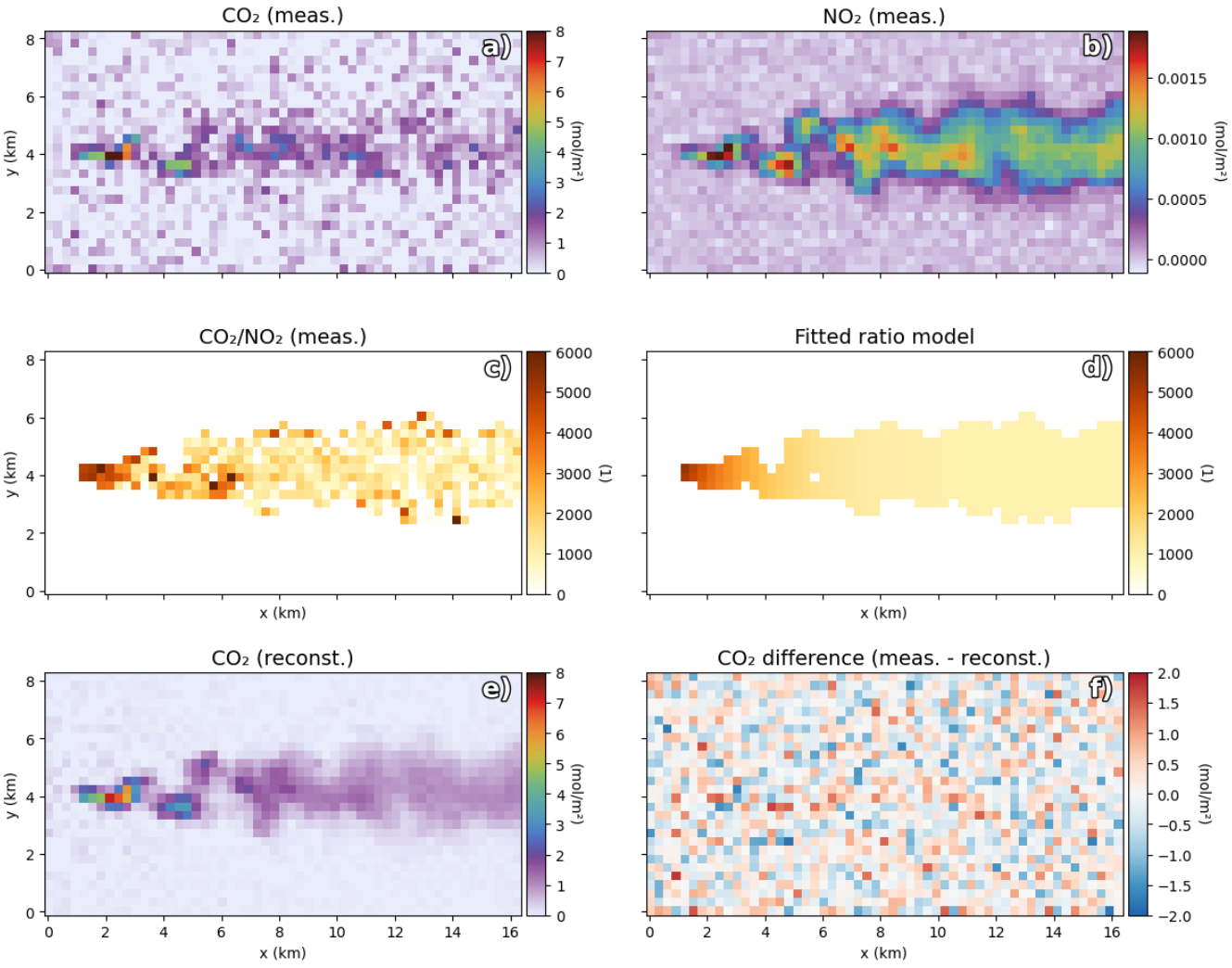

Figure 2. Demonstration of the CO_2–NO_2 plume reconstruction method using synthetic TANGO observations for the 12.5 Mt yr^{-1} CO_2 emission case. The MicroHH plume from Fig. 1 is downsampled to 300 m resolution and Gaussian noise is added (CO_2: 0.576 mol m^{-2}, NO_2: 3.75×10^{-5} mol m^{-2}). Panels show: (a) noisy CO_2 observations, (b) less noisy NO_2 observations, (c) measured CO_2/NO_2 ratio exhibiting high variability, (d) smoothed ratio from exponential model fit (Eq. 4), (e) reconstructed CO_2 field with reduced noise obtained by scaling the measured NO_2 with the fitted ratio, and (f) difference between original and reconstructed CO_2 fields, dominated by measurement noise.

https://doi.org/10.5194/egusphere-2026-1134
Preprint. Discussion started: 9 March 2026

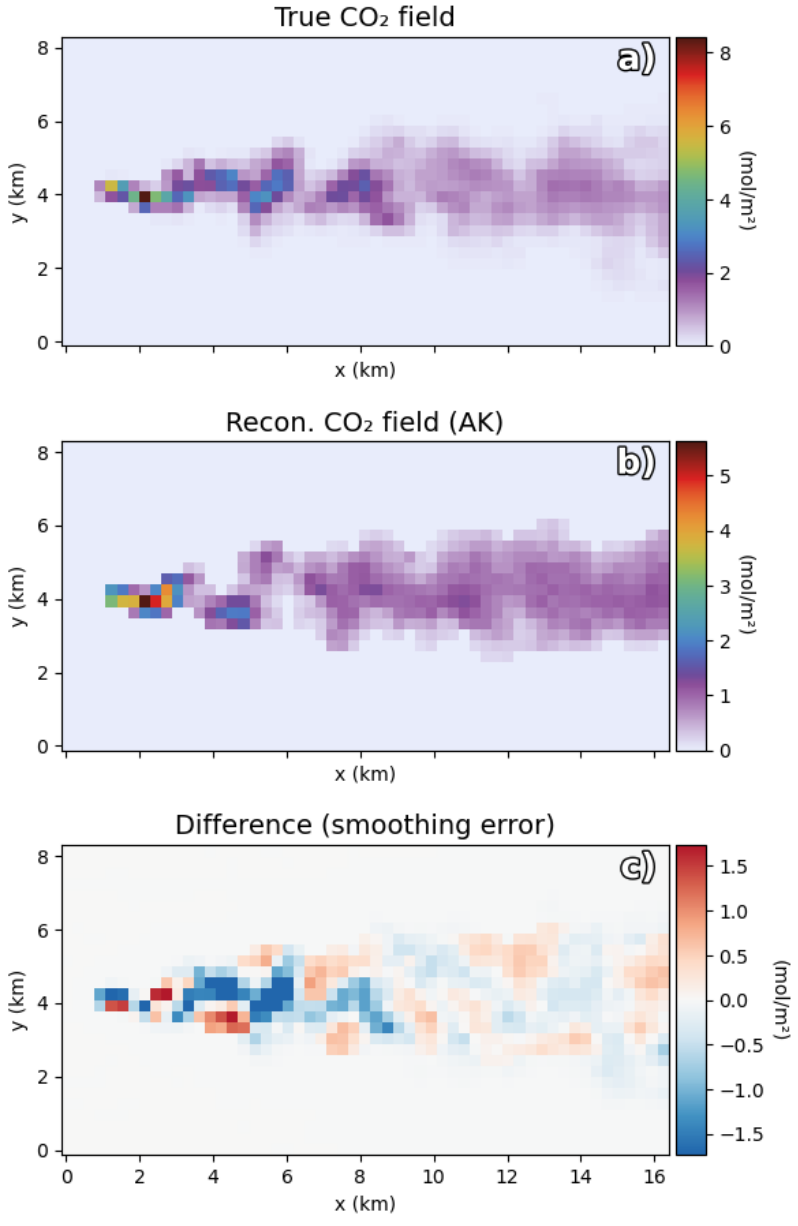

Figure 3. Application of the averaging kernel **A** for the 12.5 Mt yr^{-1} emission case demonstrating sensitivity to temporal alignment between CO_2 and NO_2 observations. (a) True CO_2 field from a plume 9 minutes before the time step used to calculate **A**. (b) Reconstructed CO_2 field when **A** (derived from the last ensemble plume) is applied to the earlier plume from panel (a) according to Eq. (15), showing turbulence patterns from the later NO_2 plume that are inconsistent with the true field in panel (a). (c) Difference between panels (b) and (a), revealing the turbulence mismatch. This demonstrates that reconstruction always responds with the turbulence features of the NO_2 field used to construct **A**, representing a fundamental limitation that requires temporal co-location between CO_2 and NO_2 observations.

https://doi.org/10.5194/egusphere-2026-1134
Preprint. Discussion started: 9 March 2026

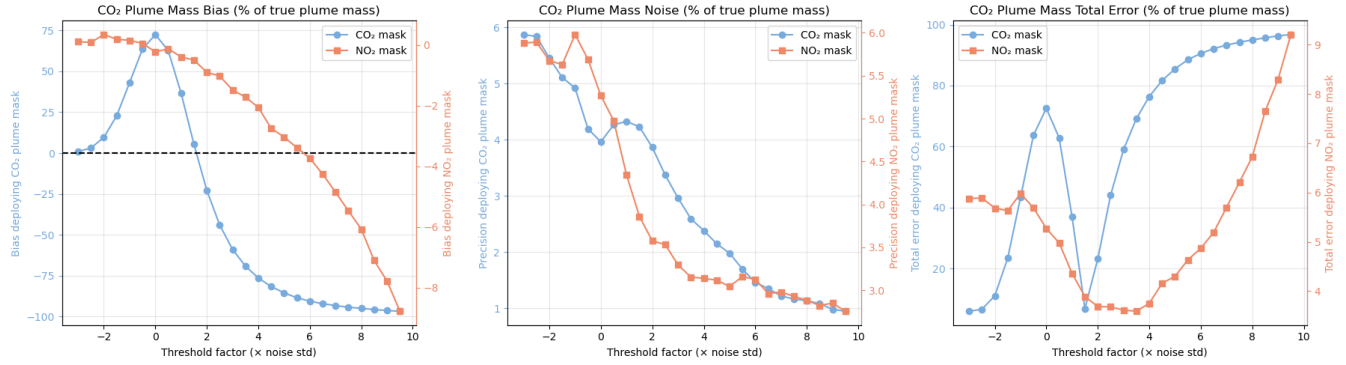

Figure 4. Trade-off between bias and noise in CO_2 plume mass estimation as a function of detection threshold for the 9 kmol s^{-1} (12.5 Mt yr^{-1}) CO_2 emission case. Two masking strategies are compared: applying a threshold to CO_2 observations (blue) versus NO_2 observations (red), with thresholds defined as multiples of the respective noise standard deviations (σ_{CO_2} = 0.576 mol m^{-2}, σ_{NO_2} = 3.75×10^{-5} mol m^{-2}). Note that the x-axis unit differs between the two curves: a threshold factor of 1 corresponds to 0.576 mol m^{-2} for CO_2 (blue) and 3.75×10^{-5} mol m^{-2} for NO_2 (red). Panels show results from Monte Carlo analysis (N=1000): (a) systematic bias in retrieved CO_2 plume mass, (b) random error (standard deviation) in mass estimates, and (c) total error ($\sqrt{\text{bias}^2+\sigma^2}$). All errors are expressed as percentage of true plume mass.

https://doi.org/10.5194/egusphere-2026-1134
Preprint. Discussion started: 9 March 2026

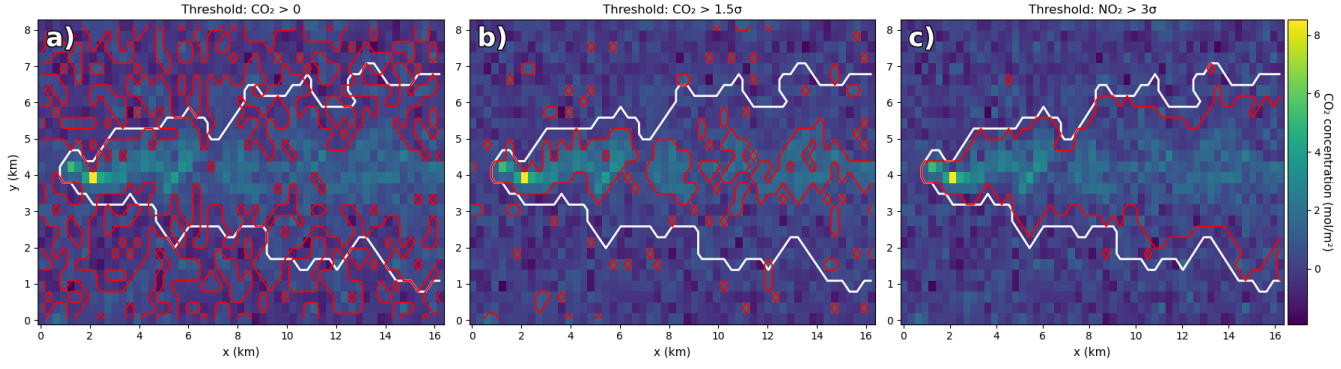

Figure 5. Illustration of plume masking for different detection thresholds for the 12.5 Mt yr^{-1} CO_2 emission case, corresponding to selected points in Fig. 4. Background colors show the CO_2 column enhancement field. The true plume mask is shown in white, while the estimated plume mask is shown in red. Panels (a) and (b) apply threshold filtering directly to CO_2 observations using the CO_2 noise standard deviation. Panel (c) applies threshold filtering to NO_2 observations, which is subsequently used as a plume mask for CO_2. The examples highlight how CO_2-based masking is increasingly affected by noise at low thresholds and by plume truncation at high thresholds, whereas NO_2-based masking provides a more spatially coherent plume delineation for comparable noise levels.

https://doi.org/10.5194/egusphere-2026-1134
Preprint. Discussion started: 9 March 2026

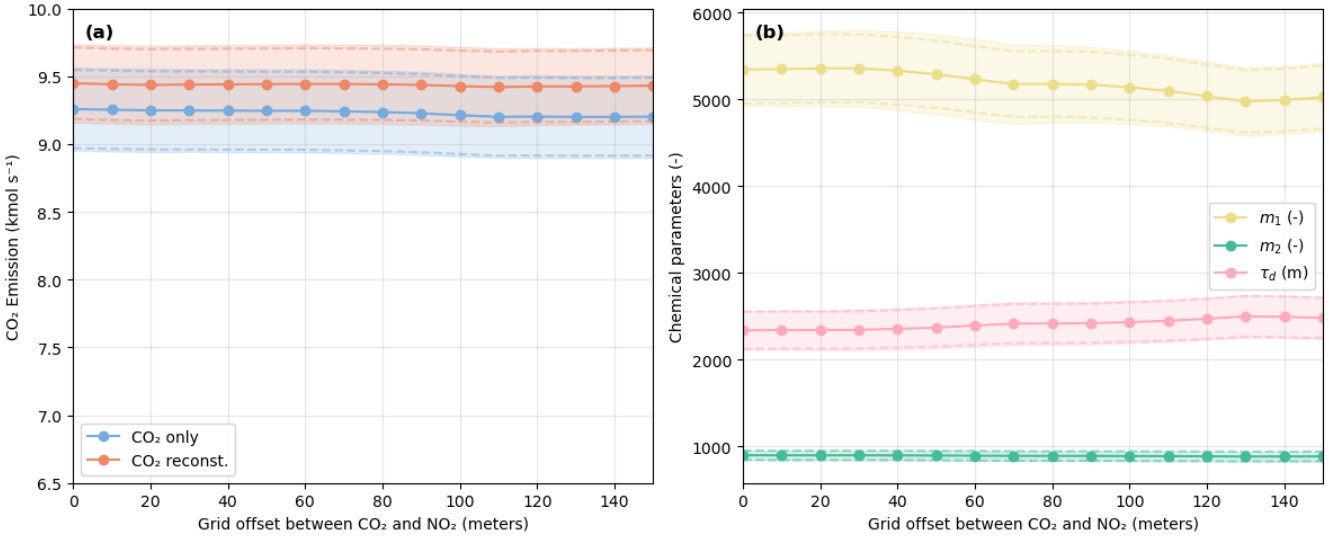

Figure 6. Robustness of emission estimates (a) and retrieved chemistry parameters $m_1 + m_0$, m_0, and τ_d (b) to spatial grid misalignment between CO_2 and NO_2 observations for the 9 kmol s^{-1} (12.5 Mt yr^{-1}) case. Monte Carlo results from 10 MicroHH plume snapshots, each combined with 500 noise realizations. Blue symbols: CO_2-only emission estimates (independent of grid shift); orange symbols: reconstructed CO_2 estimates. Error bars show Monte Carlo standard deviations; dotted lines denote analytical error estimates. Both emissions and chemistry parameters remain stable for grid offsets up to 150 m (half a TANGO pixel): emission biases stay below 2 % with ∼50 % lower uncertainties for the reconstruction, and chemistry parameters fluctuate by less than 5 %, well within their 7–10 % retrieval uncertainties.

https://doi.org/10.5194/egusphere-2026-1134
Preprint. Discussion started: 9 March 2026

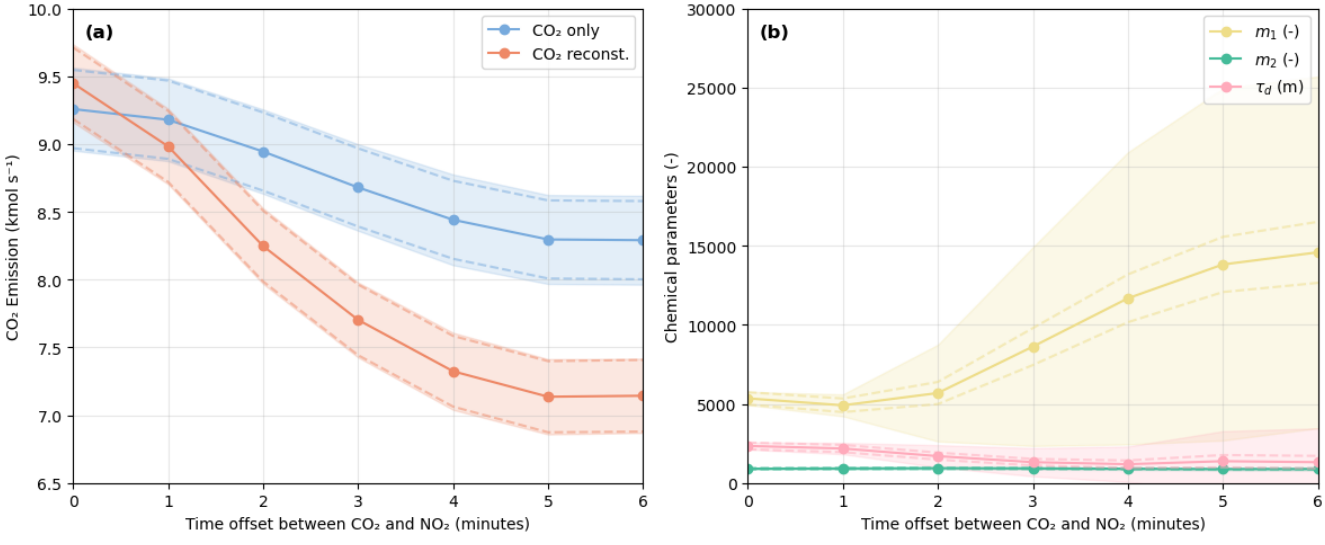

Figure 7. Robustness of emission estimates (a) and retrieved chemistry parameters $m_1 + m_0$, m_0, and τ_d (b) to temporal separation between CO_2 and NO_2 measurements for the 9 kmol s^{-1} (12.5 Mt yr^{-1}) case. Monte Carlo results from 10 MicroHH plume snapshots at 1-minute intervals, each combined with 500 noise realizations. Blue symbols: CO_2-only emission estimates (independent of temporal offset); orange symbols: reconstructed CO_2 estimates. Error bars show Monte Carlo standard deviations; dotted lines denote analytical error estimates. At TANGO's nominal 60 s separation, emission biases are below 2 % and chemistry parameters vary by less than 3 % ($m_1 + m_0$), 5 % (m_0), and 8 % (τ_d). Beyond 2 minutes, τ_d increases systematically as plume evolution introduces ratio fluctuations unrelated to chemistry, marking the practical upper limit for reliable parameter retrieval.

https://doi.org/10.5194/egusphere-2026-1134
Preprint. Discussion started: 9 March 2026

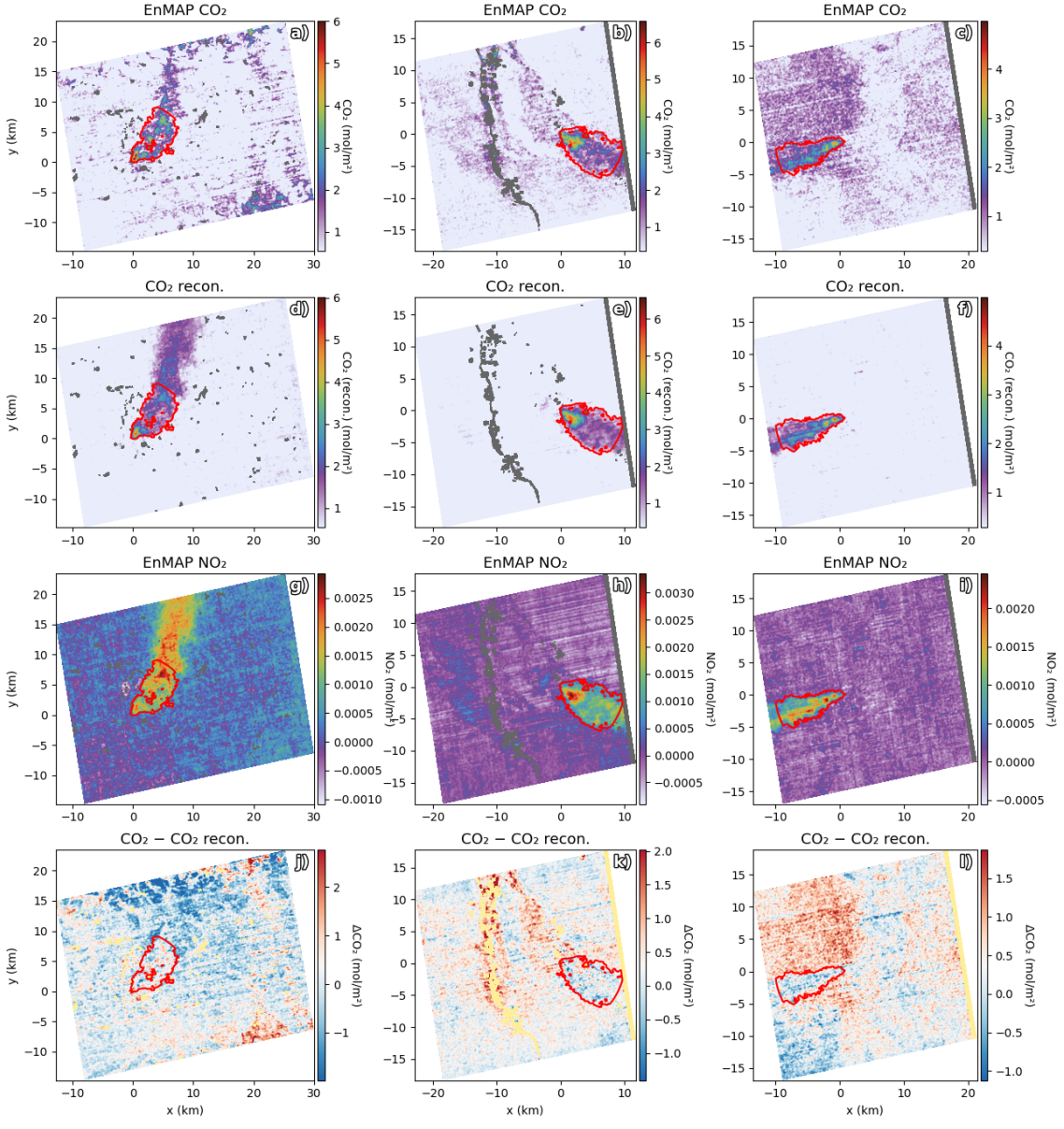

Figure 8. Application of the CO_2–NO_2 plume reconstruction method to EnMAP hyperspectral observations at 30 m spatial resolution over three industrial targets. First row (a–c): original EnMAP CO_2 retrievals showing plume structures with substantial noise and surface-related artifacts. Second row (d–f): reconstructed CO_2 fields, exhibiting reduced noise and smoother plume patterns. Third row (g–i): EnMAP NO_2 retrievals with inherently lower noise than CO_2 but some remaining artifacts, particularly visible in case (i). Fourth row (j–l): differences between original and reconstructed CO_2 fields, highlighting the noise reduction and artifact mitigation achieved by the CO_2–NO_2 plume reconstruction. Emission estimates: case 1: 19.34 kmol s^{-1} (26.9 Mt yr^{-1}) (original) vs 18.22 kmol s^{-1} (25.3 Mt yr^{-1}) (reconstructed); case 2: 34.12 kmol s^{-1} (47.4 Mt yr^{-1}) vs 32.51 kmol s^{-1} (45.2 Mt yr^{-1}); case 3: 40.04 kmol s^{-1} (55.6 Mt yr^{-1}) vs 35.72 kmol s^{-1} (49.6 Mt yr^{-1}).

https://doi.org/10.5194/egusphere-2026-1134
Preprint. Discussion started: 9 March 2026

Table 1. Comparison of emission estimates and model parameters for different CO_2 emission strengths using two approaches: (i) emission estimation from CO_2 observations using an NO_2-derived plume mask, and (ii) joint CO_2–NO_2 reconstruction. Results are shown for four emission strengths: 1.44 kmol s^{-1} (2.0 Mt yr^{-1}), 1.8 kmol s^{-1} (2.5 Mt yr^{-1}), 3.6 kmol s^{-1} (5.0 Mt yr^{-1}), and 9 kmol s^{-1} (12.5 Mt yr^{-1}). Retrieved values are shown with relative precision estimates reported as percentages: σ_{MC} denotes Monte Carlo standard deviation and $\sigma_{analytical}$ denotes the analytical error estimate. Emission bias is reported relative to the true emission. In all cases, perfect co-location in time and space between CO_2 and NO_2 observations is assumed. The last column (9 kmol s^{-1} reg) shows the joint CO_2–NO_2 reconstruction with chemical parameters fixed to values derived from noise-free simulations, illustrating the impact of parameter regularization on error characteristics.

Approach	Parameter	1.44 kmol s^{-1} (2.0 Mt yr^{-1})	1.8 kmol s^{-1} (2.5 Mt yr^{-1})	3.6 kmol s^{-1} (5.0 Mt yr^{-1})	9 kmol s^{-1} (12.5 Mt yr^{-1})	9 kmol s^{-1} (reg) (12.5 Mt yr^{-1})
CO_2 with NO_2 mask	emission (kmol s^{-1})	1.220	1.653	3.668	9.218	-
CO_2 with NO_2 mask	bias (%)	−15.3	−8.1	+1.9	+2.4	-
CO_2 with NO_2 mask	emission σ_{MC} (%)	18.5	14.0	7.6	3.4	-
CO_2 with NO_2 mask	emission $\sigma_{analytical}$ (%)	11.8	10.1	6.8	3.1	-
CO_2 / NO_2 recon.	emission (kmol s^{-1})	1.057	1.414	3.444	9.402	9.454
CO_2 / NO_2 recon.	bias (%)	−26.6	−21.4	−4.3	+4.5	+5.0
CO_2 / NO_2 recon.	emission σ_{MC} (%)	19.0	14.6	7.3	3.1	1.6
CO_2 / NO_2 recon.	emission $\sigma_{analytical}$ (%)	12.8	11.1	6.9	2.8	0.0
CO_2 / NO_2 recon.	m_1	1998.3	3732.3	3799.7	5349.5	5374.2
CO_2 / NO_2 recon.	m_1 σ_{MC} (%)	144.6	77.8	25.7	7.4	0.0
CO_2 / NO_2 recon.	m_1 $\sigma_{analytical}$ (%)	110.1	61.9	21.9	7.4	0.0
CO_2 / NO_2 recon.	m_0	1616.0	1172.4	729.9	904.3	905.0
CO_2 / NO_2 recon.	m_0 σ_{MC} (%)	21.5	15.9	14.3	6.2	0.0
CO_2 / NO_2 recon.	m_0 $\sigma_{analytical}$ (%)	17.5	14.2	12.9	5.9	0.0
CO_2 / NO_2 recon.	τ_d (m)	2196.0	1043.6	2011.2	2302.9	2312.7
CO_2 / NO_2 recon.	τ_d σ_{MC} (%)	107.0	78.3	32.3	9.7	0.0
CO_2 / NO_2 recon.	τ_d $\sigma_{analytical}$ (%)	80.1	98.4	26.3	9.2	0.0

https://doi.org/10.5194/egusphere-2026-1134
Preprint. Discussion started: 9 March 2026

Table 2. Site, observation date, wind speed, and measurement noise for CO_2 and NO_2.

Site	Date	Wind ($m\,s^{-1}$)	CO_2 noise ($mol\,m^{-2}$)	NO_2 noise ($mol\,m^{-2}$)
Matla	2023-10-05	2.79	0.65	2.92×10^{-4}
PP10	2023-07-11	4.29	0.40	1.87×10^{-4}
PP9	2023-07-15	8.76	0.44	1.22×10^{-4}

Notes: CO_2 and NO_2 noise values represent the standard deviation of background pixels in each scene, estimated from the EnMAP data as Borger et al. (2025) did not provide retrieval error estimates. These values likely underestimate true measurement uncertainty due to destriping and smoothing preprocessing applied by Borger et al. (2025).

Table 3. Emission estimates from Borger et al. (2025), original and reconstructed CO_2 fluxes, and reconstruction parameters with uncertainties.

Site	Borger et al. (2025) ($kmol\,s^{-1}$) ($Mt\,yr^{-1}$)	Original CO_2 ($kmol\,s^{-1}$) ($Mt\,yr^{-1}$)	Recon. CO_2 ($kmol\,s^{-1}$) ($Mt\,yr^{-1}$)	$m_1 + m_0$ (-)	τ_d (m)	τ_s (s)	m_0 (-)
Matla	20.23 ± 6.38 (28.1 ± 8.9)	19.34 ± 0.03 (26.9 ± 0.04)	18.22 ± 0.04 (25.3 ± 0.06)	3391 ± 39	1744 ± 32	626 ± 12	1007 ± 4
PP10	33.05 ± 13.12 (46.0 ± 18.2)	34.12 ± 0.04 (47.4 ± 0.06)	32.51 ± 0.04 (45.2 ± 0.06)	2410 ± 11	3188 ± 55	744 ± 13	941 ± 6
PP9	37.86 ± 14.64 (52.6 ± 20.4)	40.04 ± 0.06 (55.6 ± 0.08)	35.72 ± 0.06 (49.6 ± 0.08)	2834 ± 26	1451 ± 29	166 ± 3	1274 ± 3

Notes: $m_1 + m_0$ is the apparent CO_2/NO_2 source ratio, τ_d is the spatial decay scale, τ_s is the effective chemical timescale obtained by converting τ_d using wind speed, and m_0 is the background ratio. Values from Borger et al. (2025) represent cross-sectional flux estimates averaged over 10 km downwind distance for comparison with IME results. Uncertainties on reconstructed fluxes represent formal error propagation of measurement noise only and do not account for systematic errors or preprocessing-induced error correlations (see text).